

GMASS ultra-deep spectroscopy of galaxies at $z \sim 2$

II. Superdense passive galaxies: how did they form and evolve?*

A. Cimatti¹, P. Cassata², L. Pozzetti³, J. Kurk⁴, M. Mignoli³, A. Renzini⁵, E. Daddi⁶, M. Bolzonella³, M. Brusa⁷, G. Rodighiero⁸, M. Dickinson⁹, A. Franceschini⁸, G. Zamorani³, S. Berta⁶, P. Rosati¹⁰, and C. Halliday¹¹

¹ Dipartimento di Astronomia, Università di Bologna, via Ranzani 1, 40127 Bologna, Italy
e-mail: a.cimatti@unibo.it

² Laboratoire d'Astrophysique de Marseille, OAMP, UMR6110, CNRS-Université de Provence Aix-Marseille I, BP 8, 13376 Marseille Cedex 12, France

³ INAF – Osservatorio Astronomico di Bologna, via Ranzani 1, 40127 Bologna, Italy

⁴ Max-Planck-Institut für Astronomie, Königstuhl 17, 69117 Heidelberg, Germany

⁵ INAF – Osservatorio Astronomico di Padova, Vicolo dell'Osservatorio 5, 35122 Padova, Italy

⁶ CEA – Saclay, DSM/DAPNIA/Service d'Astrophysique, 91191 Gif-sur-Yvette Cedex, France

⁷ Max Planck Institut für Extraterrestrische Physik, Postfach 1312, 85741 Garching bei München, Germany

⁸ Università di Padova, Dipartimento di Astronomia, Vicolo dell'Osservatorio 2, 35122 Padova, Italy

⁹ NOAO – Tucson, 950 North Cherry Avenue, Tucson, AZ 85719, USA

¹⁰ European Southern Observatory, Karl-Schwarzschild-Strasse 2, 85748 Garching bei München, Germany

¹¹ INAF – Osservatorio Astrofisico di Arcetri, Largo E. Fermi 5, 50125 Firenze, Italy

Received 26 September 2007 / Accepted 28 December 2007

ABSTRACT

Aims. The aim of this work is to investigate the physical, structural and evolutionary properties of old, passive galaxies at $z > 1.4$ and to place new constraints on massive galaxy formation and evolution.

Methods. We combine ultra-deep optical spectroscopy from the GMASS project (*Galaxy Mass Assembly ultra-deep Spectroscopic Survey*) with GOODS multi-band (optical to mid-infrared) photometry and HST imaging to study a sample of spectroscopically identified passive galaxies at $1.39 < z < 1.99$ selected from *Spitzer Space Telescope* imaging at $4.5 \mu\text{m}$.

Results. A stacked spectrum with an equivalent integration time of ~ 500 h was obtained and compared with libraries of synthetic stellar population spectra. The stacked spectrum is publicly released. The spectral and photometric SED properties indicate very weak or absent star formation, moderately old stellar ages of ≈ 1 Gyr (for solar metallicity) and stellar masses in the range of $10^{10-11} M_{\odot}$, thus implying that the major star formation and assembly processes for these galaxies occurred at $z > 2$. No X-ray emission was found neither from individual galaxies nor from a stacking analysis of the sample. Only one galaxy shows a marginal detection at $24 \mu\text{m}$. These galaxies have morphologies that are predominantly compact and spheroidal. However, their sizes ($R_e \lesssim 1$ kpc) are much smaller than those of spheroids in the present-day Universe. Their stellar mass surface densities are consequently higher by ≈ 1 dex if compared to spheroids at $z \approx 0$ with the same mass. Their rest-frame *B*-band surface brightness scales with the effective radius, but the offset with respect to the surface brightness of the local Kormendy relation is too large to be explained by simple passive evolution. At $z \approx 1$, a larger fraction of passive galaxies follows the $z \approx 0$ size-mass relation. Superdense relics with $R_e \approx 1$ kpc are extremely rare at $z \approx 0$ with respect to $z > 1$, and absent if $R_e < 1$ kpc. Because of the similar sizes and mass densities, we suggest that the superdense passive galaxies at $1 < z < 2$ are the remnants of the powerful starbursts occurring in submillimeter-selected galaxies at $z > 2$. The results are compared with theoretical models and the main implications discussed in the framework of massive galaxy formation and evolution.

Key words. cosmology: observations – galaxies: distances and redshifts – galaxies: elliptical and lenticular, cD – galaxies: evolution – galaxies: formation – galaxies: high-redshift

1. Introduction

Deep surveys provide the observational constraints needed to understand galaxy formation and evolution. In particular, many studies have been focused on massive galaxies (i.e. stellar mass $M > 10^{11} M_{\odot}$) as cosmological probes of the history of galaxy mass assembly. However, despite the remarkable success in finding and studying massive galaxies over a wide range of cosmic time, the global picture is far from being clear. Thanks to their simple and homogeneous properties (morphology, colors, passively evolving stellar populations, scaling relations) and being

the most massive galaxies in the present-day Universe, early-type galaxies (ETGs) are crucial to investigate the cosmic history of massive galaxies (e.g. Renzini 2006, and references therein).

At $z < 1$, the most recent results seem now to agree in indicating that the majority of massive ETGs ($M > 10^{11} M_{\odot}$) were already in place at $z \approx 0.7-0.8$, with a number density consistent with the one at $z = 0$, whereas the evolution is more pronounced for the lower mass ETGs (e.g. Fontana et al. 2004; Yamada et al. 2005; Bundy et al. 2006; Cimatti et al. 2006; Borch et al. 2006; Scarlata et al. 2006; Brown et al. 2006; Bundy et al. 2007). This mass-dependent evolutionary scenario, known as “downsizing” (Cowie et al. 1996; Gavazzi & Scodreggio 1996), was proposed

* Based on the ESO VLT Large Program 173.A-0687.

to explain the galaxy star formation histories, i.e. with massive galaxies forming their stars earlier and faster than the low mass ones. Recent results suggest that the downsizing concept should extend also to the stellar mass assembly evolution itself, i.e. with massive galaxies assembling their mass earlier (e.g. Cimatti et al. 2006; Bundy et al. 2006; Franceschini et al. 2006; Bundy et al. 2007; Perez-Gonzalez et al. 2007), thus providing new and stringent constraints for the current models of galaxy formation (e.g. De Lucia et al. 2006).

The above results trace the evolution of the number density, luminosity and mass, but do not explain what is the mechanism with which ETGs assemble their mass and shape their morphology. Dissipationless ETG-ETG major merging (also called “dry” merging) has been advocated as an important mechanism to build up the masses of ETGs at $0 < z < 1$ (Bell et al. 2006; van Dokkum 2005). However, this scenario seems difficult to be reconciled with the properties of the small-scale clustering of ETGs at $0.16 < z < 0.36$ (Masjedi et al. 2006; Masjedi et al. 2007), and (for massive ETGs) with the weak evolution of the high-mass end of the stellar mass function (e.g. Cimatti et al. 2006; Bundy et al. 2006, 2007; Pozzetti et al. 2007). An alternative process proposed recently to explain the assembly of ETGs is based on multiple, frequent minor mergers at moderate redshifts (Bournaud et al. 2007).

Several studies suggest that the critical redshift range where the strongest evolution and assembly took place is at $1 \lesssim z \lesssim 2$ (e.g. Fontana et al. 2004; Glazebrook et al. 2004; Abraham et al. 2007; Arnouts et al. 2007). However, the picture at these redshifts is even more controversial than at $z < 1$, partly because of the observational difficulty to identify spectroscopically and study large samples of ETGs at $z > 1$. The few ETGs identified spectroscopically so far up to $z \approx 2.5$ are very red ($R - K > 5-6$), dominated by passively evolving old stars with ages of 1–4 Gyr, have stellar masses typically $M \gtrsim 10^{11} M_{\odot}$, and are strongly clustered with $r_0 \approx 8-10$ Mpc (Cimatti et al. 2004; Glazebrook et al. 2004; McCarthy et al. 2004; Daddi et al. 2005a; Saracco et al. 2005; Kong et al. 2006; Kriek et al. 2006). Daddi et al. (2005) were the first to realize that a large fraction of these ETGs have smaller sizes ($R_e \lesssim 1$ kpc) (see also Cassata et al. 2005) and higher mass internal densities than present-day ETGs. This result was soon confirmed by other observations (Trujillo et al. 2006; Zirm et al. 2007; Longhetti et al. 2007; Toft et al. 2007; Trujillo et al. 2007). However, it is still unclear how to explain such size-mass – density properties in the context of ETG evolution.

The existence of a substantial population of old, massive, passively evolving ETGs up to $z \approx 2$ was not predicted in galaxy formation models available in 2004–2005, and opened the question on how it was possible to assemble such systems when the Universe was so young. A promising mechanism which can provide a better agreement with the observations seems to be the “quenching” of the star formation at high redshifts with AGN “feedback” (e.g. Granato et al. 2004; Menci et al. 2006).

The stellar ages and masses of the passive ETGs at $z \approx 1-2$ require precursors characterized by strong ($>100 M_{\odot}/\text{yr}$) and short-lived (0.1–0.3 Gyr) starbursts occurring at $z > 2-3$. In addition, such precursors should also have a large clustering correlation length r_0 comparable to that of passive galaxies at lower redshifts ($z < 2$) (e.g. Daddi et al. 2000; Firth et al. 2002; Kong et al. 2006; Farrah et al. 2006), and compatible with that expected in the Λ CDM models for galaxies located in massive dark matter halos and strongly

biased environments. Examples of precursor candidates have been found amongst starburst galaxies selected at $z > 2$ with a variety of techniques (e.g. *BzK*, Daddi et al. 2004b; submm/mm, Chapman et al. 2005; “Distant Red Galaxies”, Franx et al. 2003; optically-selected systems with high luminosity, Shapley et al. 2004; IRAC Extremely Red Objects, IEROs, Yan H. et al. 2004; HyperEROs, Totani et al. 2001, and ULIRGs at $z \sim 1-3$ selected with *Spitzer Space Telescope* Berta et al. 2007). Deep integral-field near-IR spectroscopy is being used to perform detailed studies of these precursor candidates in order to understand what are the main mechanisms capable to assemble massive galaxies with short timescales (e.g. Swinbank et al. 2006; Förster-Schreiber et al. 2006; Wright et al. 2007; Law et al. 2007). To date, the most detailed case is represented by a *BzK*-selected star-forming galaxy at $z = 2.38$ which shows a massive rotating disk with high velocity dispersion which may become unstable and lead to the rapid formation of a massive spheroid (Genzel et al. 2006).

In this paper, we exploit the combination of GMASS ultra-deep spectroscopy, HST imaging and optical – to – mid-infrared photometry to study the global properties of a new sample of passive galaxies at $1.3 < z < 2.0$ in order to place new constraints on massive galaxy formation and evolution. This paper refers to other papers where more details can be found on the GMASS project (Kurk et al. 2007a, in preparation), the large scale structure at $z = 1.61$ (Kurk et al. 2007b, in preparation), the photometric Spectral Energy Distribution (SED) fitting analysis (Pozzetti et al. 2007, in preparation) and the morphological analysis (Cassata et al. 2007, in preparation). We adopt $H_0 = 70 \text{ km s}^{-1} \text{ Mpc}^{-1}$, $\Omega_m = 0.3$ and $\Omega_{\Lambda} = 0.7$, give magnitudes in AB photometric system, and assume a Chabrier (2003) Initial Mass Function (IMF).

2. The GMASS sample

GMASS (“Galaxy Mass Assembly ultra-deep Spectroscopic Survey”¹) is a project based on an ESO VLT Large Program (Kurk et al. 2007a).

The GMASS main scientific driver is to investigate the physical and evolutionary processes of galaxy mass assembly in the redshift range of $1.5 < z < 3$, i.e. in the epoch when the crucial processes of massive galaxy formation took place. Photometric redshifts are not sufficient to fully address the above questions because they provide limited clues on the physical and evolutionary status of the observed galaxies. Spectroscopy is therefore essential to derive reliable spectroscopic redshifts, to perform detailed spectral and photometric SED fitting (with known spectroscopic redshift), and to characterize the nature and diversity of galaxies at $1.5 < z < 3$.

The first step was to select a sample at $4.5 \mu\text{m}$ by using the GOODS-South public image taken at that wavelength with the *Spitzer Space Telescope* equipped with IRAC (Dickinson et al., in preparation). Firstly, we defined a region of $6.8 \times 6.8 \text{ arcmin}^2$ (matching the field of view of FORS2) located within the GOODS-South field², and covering $\sim 80\%$ of the *Hubble Ultra Deep Field* (HUDF) (Beckwith et al. 2006). Secondly, the sample was selected by extracting *all* the sources present in that field and having $m_{4.5} < 23.0$ (AB) (corresponding to a flux density $> 2.3 \mu\text{Jy}$). This selection provided 1094 objects belonging to what we call the GMASS sample, which is clearly a

¹ <http://www.arcetri.astro.it/~cimatti/gmass/gmass.html>

² <http://www.stsci.edu/science/goods>

pure flux-limited sample. Extended simulations showed that at $m_{4.5} < 23.0$, the photometric completeness is $\sim 85\%$ (Dickinson & Rodighiero, private communications).

The GMASS sample was then used to extract a sub-sample of target galaxies to be observed spectroscopically. To reach the GMASS scientific aims, spectroscopy was very deep in order to derive secure spectroscopic redshifts for the faintest galaxies and to obtain high-quality spectra for the brighter galaxies in order to allow detailed spectral studies. The GMASS optical multi-slit spectroscopy was done with the ESO VLT + FORS2 (MXU mode) and focused on galaxies pre-selected with a cut in photometric redshift of $z_{\text{phot}} > 1.4$ in order to concentrate the study on galaxies in the critical range of $1.5 < z < 3$. In order to make the spectroscopy feasible, two cuts in the optical magnitudes were adopted: $B < 26.5$ or $I < 26.5$ for spectroscopy done in the blue (grism 300V) or in the red (grism 300I) respectively. The integration times were very long (up to 32 h per spectroscopic mask), and the spectroscopy was optimized by obtaining spectra in the blue (4000–6000 Å, grism 300V) or in the red (6000–10000 Å, grism 300I) depending on the colors and photometric SEDs of the targets. For both grisms, the slit width was always 1 arcsec and the spectral resolution $\lambda/\Delta\lambda \approx 600$. Despite the faintness of the targets, GMASS spectroscopy provided an overall spectroscopic redshift success rate of about 85% for the targeted galaxies.

Overall, $\approx 50\%$ of the GMASS flux-limited sample ($m_{4.5} < 23.0$) has available spectroscopic redshifts if we combine our own spectroscopy with the literature redshifts (<http://archive.eso.org/archive/adp/GOODS>), whereas the other half has accurate photometric redshifts (see Kurk et al. 2007a).

In summary, the GMASS sample is a pure flux-limited sample selected with $m_{4.5} < 23.0$, and with spectroscopic (GMASS or literature) or photometric redshifts available for each object in the sample. The power and the novelty of the GMASS sample is the selection at $4.5 \mu\text{m}$, which is crucial for two main reasons: (1) the peak of the stellar SEDs ($\lambda_{\text{rest}} = 1.6 \mu\text{m}$) is redshifted in the $4.5 \mu\text{m}$ band for $z > 1.5$, (2) it is sensitive to the rest-frame near-IR emission, i.e. to stellar mass, up to $z \approx 3$. For $m_{4.5} < 23.0$ and a Chabrier IMF, the limiting stellar mass is $\log(M/M_{\odot}) \approx 9.8, 10.1, \text{ and } 10.5$ for $z \approx 1.4, z \approx 2, \text{ and } z \approx 3$, respectively. This allows to properly investigate the galaxy mass assembly evolution within a wide range of masses.

3. Passive galaxies in the GMASS sample

3.1. Spectroscopic selection and properties

At each redshift, the oldest envelope of the galaxy population is a “fossil” tracer of past events of galaxy formation in a way complementary to the study of galaxies with ongoing star formation. ETGs can be used as “fossil” probes as they are usually dominated by old, passively evolving stellar populations.

The rest-frame UV spectra of old and passive stellar populations have specific features different from those of younger or star-forming galaxies. The UV continuum is very red, characterized by prominent breaks at 2640 Å and 2900 Å and rich of metal absorptions (e.g. MgI $\lambda 2852$, MgII $\lambda 2800$, FeI and FeII lines) (e.g. Dunlop et al. 1996; Spinrad et al. 1997; Cimatti et al. 2004; Saracco et al. 2005; Daddi et al. 2005a). The combination of the strongest breaks and absorptions at 2600–2900 Å produces the prominent Mg_{UV} feature (Daddi et al. 2005a). The presence of this feature in a galaxy spectrum ensures that very little if any star formation has taken place over the last ~ 0.5 Gyr, and therefore the galaxy is in a

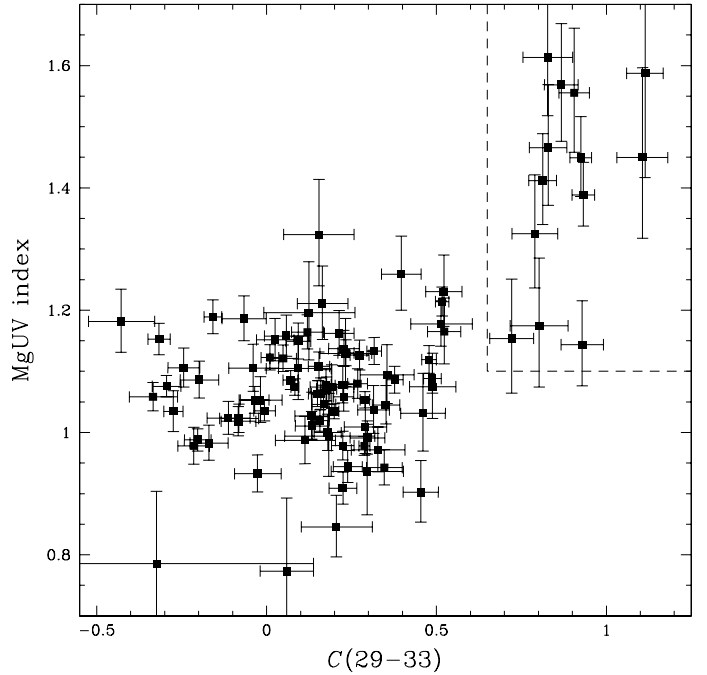


Fig. 1. The Mg_{UV} index vs. the UV color index defined in the text, for the GMASS galaxies with $z > 1$. All the selected high- z passive galaxies fall within the box in the upper-left corner of the plot, having a distinctively red UV color index. Also, all but three galaxies show a Mg_{UV} index greater than 1.2, typical of an evolved stellar population (see Daddi et al. 2005).

passively evolving stage. This feature is also very important to measure the spectroscopic redshifts of this kind of galaxies using optical spectrographs, when for $z > 1.4$ the more prominent features of ETGs such as the CaII H&K doublet and the Balmer/4000 Å breaks fall outside the optical spectral range.

Following this approach, the GMASS spectroscopic dataset was used to search for passively evolving galaxies at $z > 1.4$ with the Mg_{UV} feature present in their spectra (Mignoli et al., in preparation). This was achieved by deriving a color index of the UV continuum of each GMASS galaxy with available spectrum and spectroscopic redshift $z > 1$, and searching for the red continuum spectra expected in the case of passive galaxies. This UV color was defined as:

$$C(29 - 33) = -2.5 \log[F_{\nu}(2900)/F_{\nu}(3300)]$$

where $F_{\nu}(2900)$ and $F_{\nu}(3300)$ are the mean spectral continuum flux densities within the rest-frame wavelength bins at 2700–3100 Å and 3100–3500 Å respectively. The continuum flux densities were measured in fixed rest-frame spectral ranges and adopting a *sigma-clipping* procedure which ensures that spikes due to bad sky subtraction and/or to cosmic rays residuals do not affect the measured values. The errors were then computed from the standard deviations.

Figure 1 shows that a strong color segregation is present, with 13 galaxies at $1.39 < z < 1.99$ having $C(29-33)$ significantly redder than the rest of the GMASS spectroscopic sample. These red galaxies have also a Mg_{UV} index in the range expected for passive galaxies (Daddi et al. 2005a). The visual inspection of these 13 spectra confirmed their similarity with the spectra of LBDS 53w091 (see Fig. 1) (Dunlop et al. 1996; Spinrad et al. 1997) and of old passive galaxies at $z > 1$ taken from the K20 and GDDS surveys (Mignoli et al. 2005; Cimatti et al. 2004; McCarthy et al. 2004).

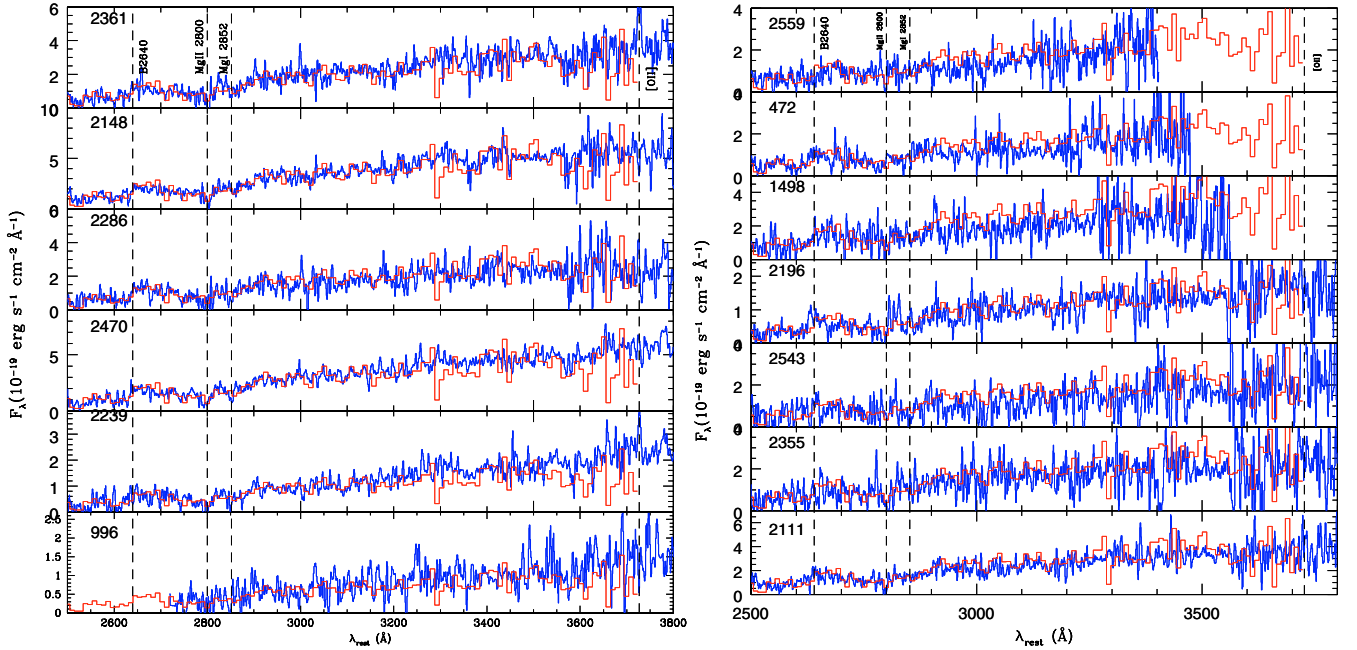


Fig. 2. The individual spectra of the selected galaxies ordered with increasing redshift from bottom to top in each panel. The red line is the spectrum of the old galaxy LBDS 53w091 ($z = 1.55$; Dunlop et al. 1996; Spinrad et al. 1997) used to search for spectra with a similar continuum shape.

Table 1. The sample of passive galaxies.

ID	Coordinates (J2000)	$m_{4.5}$	I	K_s	$B - z$	$z - K_s$	spec- z	$F_{\text{obs}}([\text{O II}]\lambda 3727)$ $\times 10^{-18} \text{ erg s}^{-1} \text{ cm}^{-2} \text{ \AA}^{-1}$	$EW_{\text{obs}}([\text{O II}]\lambda 3727)$ \AA
472	53.1588440 -27.7971249	21.04	25.29	21.72	3.25	2.57	1.921	–	–
996	53.1538162 -27.7745972	21.36	25.27	22.02	3.57	2.27	1.390	<1	<7
1498	53.1746445 -27.7533722	20.72	25.35	21.57	2.54	2.80	1.848	–	–
2111	53.1164055 -27.7126999	20.64	24.58	21.31	3.99	2.52	1.610	<2	<6
2148	53.1512375 -27.7137375	19.80	24.17	20.50	4.57	2.71	1.609	<2	<5
2196	53.1527710 -27.7162437	20.34	24.53	20.92	4.28	2.51	1.614	<2	<10
2239	53.1304817 -27.7211590	20.61	24.53	21.24	4.08	2.39	1.415	4.0 ± 0.5	22 ± 4
2286	53.1249580 -27.7229443	20.82	25.08	21.55	3.69	2.53	1.604	3.5 ± 0.5	29 ± 5
2355	53.0596466 -27.7258034	20.93	24.83	21.78	2.90	2.30	1.610	<2	<9
2361	53.1085548 -27.7101574	20.40	24.90	21.10	4.08	2.71	1.609	8.0 ± 1.0	26 ± 4
2470	53.1421547 -27.7112675	20.16	23.70	20.68	3.85	2.14	1.416	<2	<4
2543	53.1496468 -27.7113838	20.26	25.24	21.25	3.40	3.20	1.612	15.0 ± 5.0	100 ± 40
2559	53.1764069 -27.7011585	20.71	24.84	21.60	3.37	2.81	1.981	–	–

All the other GMASS spectra of galaxies at $z > 1$ were visually inspected in order to check for other passive/red galaxies with spectra that may have missed by the UV color criterion, but no other cases were found. The question of how many other red/passive ETGs are present in the *whole* GMASS flux-limited sample (i.e. including also galaxies with only photometric redshifts) is beyond the scope of the present work and is being addressed in another paper (Cassata et al. 2007, in preparation).

The spectra of the 13 selected galaxies are shown in Fig. 2 and some properties are listed in Table 1. Seven of these galaxies belong to a large scale structure at $z = 1.61$ that is discussed in a companion paper (Kurk et al. 2007b). Ten spectra were obtained with an integration time of 30 h each, whereas three (IDs 2111, 2239, 2559) were repeated in two independent masks and each of them accumulated an integration time of 60 h. The two galaxies located within the HUDF (IDs 472 and 996) were also consistently identified by Daddi et al. (2005a) (their IDs 3650 and 8238 respectively) using HST+ACS slitless grism spectroscopy (GRAPES project; Pirzkal et al. 2004).

Six spectra show no signs of star formation due to the lack of [O II] $\lambda 3727$ emission, four have weak [O II] emission, and

for the three galaxies at $z > 1.8$ (IDs 472, 1498, 2559) there is no information on [O II] $\lambda 3727$ because the line falls outside the observed spectral range. Assuming that the [O II] emission line fluxes (Table 1) are not due to an AGN, and using the conversion from [O II] $\lambda 3727$ luminosity and star formation rate (*SFR*) of Kennicutt (1998), we derive $SFR \approx 1\text{--}4 M_{\odot} \text{ yr}^{-1}$ for the four galaxies with [O II] $\lambda 3727$ emission (see Table 1). If dust extinction is present, these *SFR*s are lower limits. However, the similarity of the spectra of these four galaxies with the spectra of galaxies without line emission suggests that the bulk of the stars is made by old stellar population and that the [O II] $\lambda 3727$ emission is probably due to a minor episode of star formation (see also Sect. 5.2 on the specific star formation rate), or to weak nuclear activity.

While the presence of type 1 AGN is excluded by the lack of broad emission lines (e.g. MgII $\lambda 2800$), we cannot rule out the presence of hidden AGN activity. For instance, Yan et al. (2006) found that a large fraction of SDSS galaxies at $z < 0.1$ with red rest-frame colors and emission lines display line ratios typical of various types of AGNs (LINERs, transition objects, and, more rarely, Seyferts) rather than of star-forming galaxies.

In the case of our spectra, emission line ratio studies are not possible because the relevant lines fall outside the observed range. This implies that the above $SFRs$ could be taken as upper limits. However, the lack of high ionization lines (e.g. $[NeV]\lambda 3426$) makes the AGN hypothesis unlikely. The presence of hidden luminous AGNs is also excluded by the stacking analysis of the X-ray data (see Sect. 4). Therefore, we conclude that the $[OII]$ emission in these 4 galaxies is likely due to a very low level of ongoing star formation.

In the present paper, we focus the analysis on these 13 galaxies for which ultradeep GMASS spectra are available. We only mention here that other passive galaxy *candidates* are present in the GMASS sample in the same redshift range. However, no spectroscopic redshifts are available for these candidates and their properties are based only on the similarity of their SED fitting parameters with those of the 13 spectroscopic passive galaxies discussed here (see Sect. 5.2). The detailed study of these candidates will be the subject of a forthcoming paper (Cassata et al. 2007, in preparation).

3.2. Analysis of the 480-h stacked spectrum

The availability of deep individual spectra provides the opportunity to add them together and to obtain a *stacked* spectrum with unprecedented depth and suitable for a detailed analysis. We emphasize that the GMASS stacked spectrum of the 13 ETGs has an equivalent integration time of $(10 \times 30 \text{ h}) + (3 \times 60 \text{ h}) = 480 \text{ h}$ (1.73 Ms). The need for such extremely long integration times highlights the limits of the current generation of 8–10 m telescopes in obtaining spectra of red passive galaxies with faint optical magnitudes down to $I \approx 25\text{--}26$. Moreover, near-infrared continuum and absorption line spectroscopy of this kind of galaxies with $K_s \gtrsim 21$ is beyond the current limits of 8–10 m telescopes. Thus, these galaxies are ideal targets for the next generation of large telescopes on the ground (e.g. E-ELT, TMT) and in space (JWST).

The stacked spectrum shown in Figs. 3–4 was obtained by averaging all the 13 individual spectra (average redshift $\langle z \rangle = 1.6$). In particular, each spectrum was blue-shifted to the rest-frame according to its redshift (with a 1.0 \AA rest-frame bin) and normalized in the 2600–3100 \AA wavelength range, which is always covered in the observed spectral window. In order to avoid any bias towards the brightest galaxies with the highest S/N ratio, the same weight was assigned to each individual spectrum. The main features present in the stacked spectrum are listed in Table 2. The stacked spectrum is publicly available at <http://www.arcetri.astro.it/~cimatti/gmass/gmass.html>.

Figure 3 shows a comparison between the average spectrum of all 13 GMASS ETGs and those of K20 (Cimatti et al. 2004) and GDDS (McCarthy et al. 2004) samples. With the exception of the composite GDDS spectrum at $1.6 < z < 1.9$ (slightly bluer and with less pronounced Mg_{UV} feature), the spectra are very similar to each other both in the strength of the Mg -UV feature and continuum slope.

The observed average spectrum was compared to various libraries of synthetic spectra of simple stellar populations (SSPs) in order to attempt an estimate of the age of the stellar population dominating the rest-frame UV spectrum covered by our observations. In practice, limiting the analysis to this part of the spectrum provides an estimate of the time elapsed since the last major episode of star formation. As such, this estimate must be

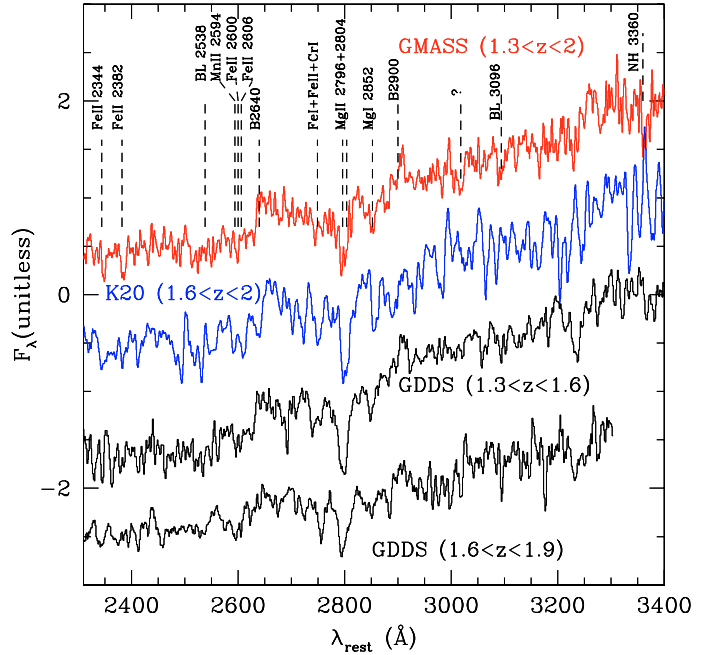


Fig. 3. Comparison of rest-frame UV spectra of passively evolving galaxies from GMASS (this work), K20 (Cimatti et al. 2004) and GDDS (McCarthy et al. 2004) surveys.

regarded as a *lower* limit to the age of the bulk of the stars in these galaxies. As a second step we included also the rest-frame near-IR, so as to have an estimate of the age of the bulk stellar populations in these galaxies (see Sect. 5.2).

For the fitting analysis, we adopted three libraries of synthetic spectra: Maraston (2005, M05) (Kroupa 2001, IMF), Bruzual & Charlot, BC03) (Chabrier, IMF), and its update (Charlot & Bruzual 2007; CB07) (Chabrier, IMF). The main difference among the three sets of models is in the treatment of the thermally pulsing asymptotic giant branch (TP-AGB) phase of stellar evolution, which for intermediate age SSPs can contribute up to $\sim 50\%$ to the total bolometric light, radiated mostly in the near-IR (Renzini 1981; Maraston 1998, 2005; Maraston et al. 2006). In M05 models the TP-AGB contribution was calibrated using Magellanic Cloud globular clusters of various ages, whereas BC03 models had a negligibly small contribution of the TP-AGB at all ages (M05). With CB07 an attempt was made to obviate to this deficiency (Bruzual 2007). We concentrate here on the analysis of the rest-frame UV spectrum alone, for which the TP-AGB contribution is irrelevant, postponing to Sect. 5.2 the inclusion of the whole photometric information on these galaxies, including the rest-frame near-IR.

The BC03 and CB07 models have a spectral resolution of $\lambda/\Delta\lambda \sim 300$ (i.e. $\sim 10 \text{ \AA}$) for $\lambda < 3300 \text{ \AA}$ and $\Delta\lambda \sim 3 \text{ \AA}$ for $\lambda > 3300 \text{ \AA}$, whereas the M05 spectra have $\lambda/\Delta\lambda \sim 300$ at all wavelengths. The observed stacked spectrum (resolution $\lambda/\Delta\lambda \sim 600$, i.e. $\Delta\lambda \sim 2 \text{ \AA}$ at $\lambda_{\text{rest}} = 3000 \text{ \AA}$, $\langle z \rangle = 1.6$) was rebinned to match the resolution of the model spectra.

The best fit age for each set of synthetic templates was derived through a χ^2 minimization over the rest-frame wavelength range 2480–3560 \AA that is covered completely by 11 out of the 13 spectra. The rms as a function of wavelength used in the χ^2 procedure was estimated from the average spectrum computing a running mean rms within 20 \AA and 10 \AA for $\lambda < 3300 \text{ \AA}$ and $\lambda > 3300 \text{ \AA}$ respectively. All ages available in the model spectra

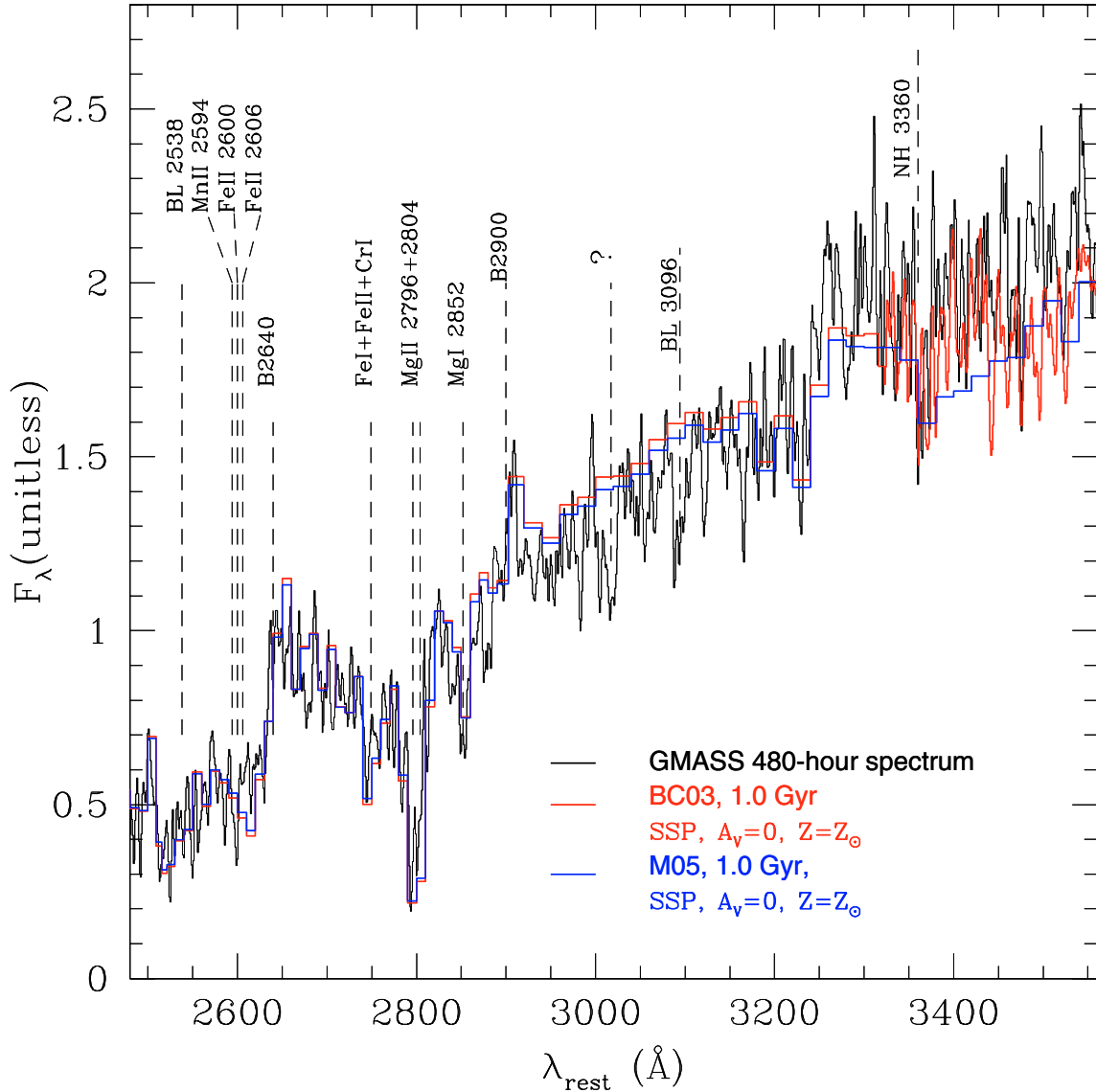


Fig. 4. The average spectrum of GMASS passive galaxies (black) and two synthetic spectra which provide the formal best fit in the range of 2480–3560 Å for solar metallicity and age of 1.0 Gyr for all the models (BC03 and M05). The CB07 best fitting spectrum is not shown because it is identical to the BC03 one. The question mark indicates an unidentified absorption feature at ~ 3018 Å. The stacked spectrum is publicly available at <http://www.arcetri.astro.it/~cimatti/gmass/gmass.html>.

libraries were used, and we initially adopted $A_V = 0$ during the fitting.

In the case of solar metallicity, the best fitting spectra have an age of 1.0 Gyr for all models (BC03, M05 and CB07) (Fig. 4), indicating the three sets of models are virtually equivalent in this wavelength range (BC03 and CB07 are actually identical, the only difference being at longer wavelengths).

In order to assess the relevance of the age-metallicity degeneracy, we explored how the estimated age changes as a function of metallicity Z with BC03/CB07 models. This was done by assuming no dust extinction ($A_V = 0$) and evaluating how the best-fitting age changes as a function of Z using six values of metallicity: $Z = 0.0004, 0.001, 0.004, 0.008, 0.019, 0.03$. We found that the best-fit ages vary from 0.7 Gyr to 2.8 Gyr for $Z = 1.5\text{--}0.2 Z_\odot$. Lower metallicities ($Z < 0.2 Z_\odot$) are excluded because they never reproduce the observed spectrum. Although the results of the SED fitting (see Sect. 5.2) exclude the presence of substantial dust extinction (not surprisingly, as most of the sample galaxies show no or very weak star formation), we

also studied the effects of including the dust attenuation in the fitting process. This was done by leaving the stellar age and the dust extinction (A_V) as free parameters for each fitting done with a fixed metallicity Z (with $0.0004 \leq Z \leq 0.03$, with the same six metallicity values as above). The dust extinction was allowed to vary in the range of $0 \leq A_V \leq 0.6$ in order to be consistent with the results of the SED fitting of Sect. 5.2. Compared to the case with no dust extinction ($A_V = 0$), the best-fitting ages were found to slightly decrease to 0.6–2.3 Gyr for $Z = 1.5\text{--}0.2 Z_\odot$. This exercise clearly showed that the dominant degeneracy is the one of age and metallicity, which become substantial when using the UV spectrum alone.

We note that in all cases, the oldest acceptable ages never exceed the age of the Universe (3.27 Gyr) at the redshift ($z = 1.981$) of the most distant galaxy in the stacked spectrum. Figure 4 shows the best-fitting model spectra (for $Z = Z_\odot$) and the observed stacked spectrum. However, Fig. 5 shows that the same model spectra which provide equally good fits in the rest-frame UV differ significantly at longer wavelengths (see also

Table 2. Spectral features in the stacked spectrum.

Feature	Value	Type	Reference
FeII 2344	$4.5 \pm 0.3 \text{ \AA}$	Equivalent Width	Ponder et al. (1998)
FeII 2382	$6.0 \pm 0.4 \text{ \AA}$	Equivalent Width	Ponder et al. (1998)
BL 2538	$5.0 \pm 1.0 \text{ \AA}$	Equivalent Width	Ponder et al. (1998)
B2640	1.59 ± 0.06	Continuum Break	Spinrad et al. (1997)
B2900	1.27 ± 0.03	Continuum Break	Spinrad et al. (1997)
MgII 2800	$8.0 \pm 0.6 \text{ \AA}$	Equivalent Width	Ponder et al. (1998)
MgI 2852	$8.0 \pm 0.6 \text{ \AA}$	Equivalent Width	Ponder et al. (1998)
BL 3096	$2.5 \pm 0.5 \text{ \AA}$	Equivalent Width	Ponder et al. (1998)
NH 3360	$2.5 \pm 0.4 \text{ \AA}$	Equivalent Width	Ponder et al. (1998)
Mg _{UV}	1.40 ± 0.1	Continuum Break	Daddi et al. (2005)

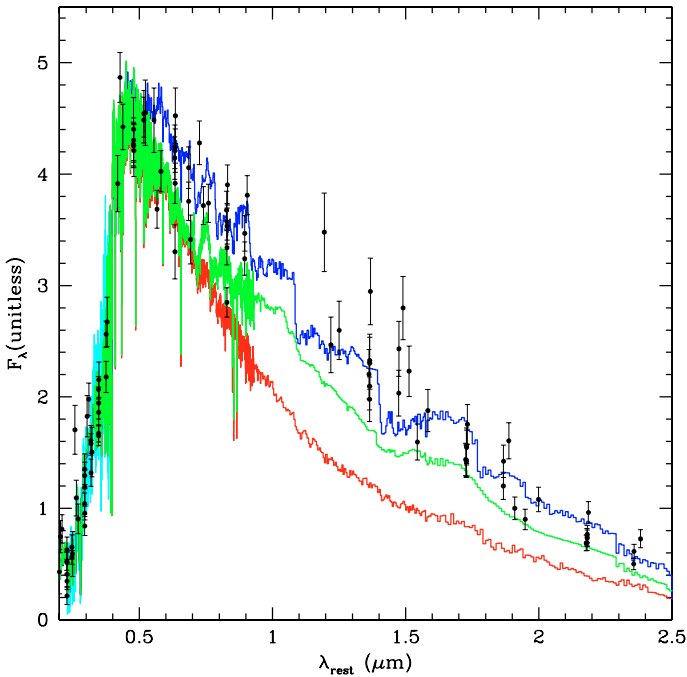


Fig. 5. Same as in Fig. 4, but including also the CB07 best fitting spectrum (green) and showing how the templates differ with each other at longer wavelengths. The observed stacked spectrum is shown in cyan. The black dots are the rest-frame photometry of the galaxies normalized at $\lambda_{\text{rest}} = 0.5 \mu\text{m}$ (see text for more details).

Maraston et al. 2006). Figure 5 shows also the “stacked” photometric SED obtained by de-redshifting the multi-band photometry ($BVIzJHK_s + 3.6 \mu\text{m}, 4.5 \mu\text{m}, 5.8 \mu\text{m}, 8 \mu\text{m}$) of each galaxy and normalizing it to the average flux of the three SSP spectra at $\lambda_{\text{rest}} = 0.5 \mu\text{m}$, a wavelength at which all the three model spectra are nearly identical. The photometry of ID 2543 was excluded because significantly redder from the SEDs of the other 12 galaxies at $\lambda_{\text{rest}} > 1 \mu\text{m}$. Figure 5 shows that for the three different SSP spectra with a fixed age of 1 Gyr, the “stacked” photometric SED is in better agreement with the M05 model (although the scatter in the photometry is significant). The same figure also clearly suggests that more stringent constraints on the stellar population content of the passive galaxies come from the photometric SED fitting analysis extended to the *Spitzer Space Telescope* IRAC bands. This is discussed in details in Sect. 5.2.

4. X-ray and $24 \mu\text{m}$ emission

In order to search for additional indicators of “activity” due to hidden star formation and/or AGN, we explored whether the

13 passive galaxies were detected in the X-ray or $24 \mu\text{m}$ data using the Chandra X-ray Observatory and the *Spitzer Space Telescope* + MIPS data publicly available for the GOODS-South/GMASS region.

X-ray data for a total exposure time of ~ 1 Ms obtained with the *Chandra* observatory in the GOODS/CDFS field have been published and made publicly available by Giacconi et al. (2002, see also Alexander et al. 2003). The limiting flux of the X-ray data is $\sim 1 \times 10^{-16} \text{ erg cm}^{-2} \text{ s}^{-1}$ in the full band at 0.5–7 keV. We searched for individual emission from the 13 objects in the present sample by cross-correlating the IRAC positions of our targets with the positions of X-ray sources as catalogued by Giacconi et al. (2002) and Alexander et al. (2003). We found that none of the 13 sources was individually detected in the X-rays. In order to constrain the average X-ray properties of our sample galaxies, we used the “stacking technique” following Brusa et al. (2002). For the photometry, a circular aperture with a radius of $2''$ centered at the positions of our sources was adopted. The counts were stacked in the standard soft, hard and full bands (0.5–2 keV, 2–7 keV, and 0.5–7 keV) for a total effective exposure time of ≈ 11 Ms. Extensive Monte Carlo simulations (up to 10 000 trials) have been carried out by shuffling 13 random positions and using the same photometry aperture (2 arcsec). The random positions were chosen to lie in “local background regions” to reproduce the actual background as close as possible. In none of the bands (full, hard, soft), a signal has been significantly detected. The background counts at 0.5–2 keV imply a count rate of $< 5.2 \times 10^{-6} \text{ counts s}^{-1}$ and a flux $< 3 \times 10^{-17} \text{ erg cm}^{-2} \text{ s}^{-1}$ assuming an unobscured $\Gamma = 2.0$ power-law spectrum. This implies upper limits on the rest-frame luminosity of $< 5.2 \times 10^{41} \text{ erg s}^{-1}$ at 0.5–2 keV. These limits imply that a luminous AGN source ($L_X > 10^{42} \text{ erg s}^{-1}$) is absent in the passive galaxies of our sample or is very heavily obscured.

Around $z \approx 1$, about 20% of the morphologically-selected ETGs show some level of “hidden” activity revealed through the mid-IR emission at $24 \mu\text{m}$ (Rodighiero et al. 2007). Mid-infrared emission was searched using the public data available for GOODS-South obtained with *Spitzer* + MIPS at $24 \mu\text{m}$ with an integration time of about 10 h per sky pixel. The photometry was based on a PSF fitting algorithm, where the *SExtractor* (Bertin & Arnouts 1997) positions of the IRAC sources were used as input to the MIPS source extraction process (Chary et al. in preparation; see also Daddi et al. 2007a,b for more details). None of the 13 galaxies is a strong MIPS source. The fluxes of 12 galaxies are not significant ($< 2-3\sigma$) and $F_{24} < 20 \mu\text{Jy}$. The only exception is object ID 2543 which has a possible detection at 4.7σ significance level with a flux $F(24) = 24.7 \pm 5.3 \mu\text{Jy}$. We recall that ID 2543 is also the galaxy with the strongest [OII] $\lambda 3727$ emission. If the $24 \mu\text{m}$ emission is real and due to star formation activity, and extrapolating from the $24 \mu\text{m}$ measurements using the spectral templates of Chary & Elbaz (2001; see for instance Daddi et al. 2007a,b, the implied infrared (bolometric) luminosity is $\approx 1.4 \times 10^{11} L_\odot$. If we convert this luminosity into a *SFR* using the recipe of Kennicutt (1998), we obtain $\approx 24 M_\odot \text{ yr}^{-1}$, higher than the estimate based on [OII] $\lambda 3727$ luminosity ($4 M_\odot \text{ yr}^{-1}$) or SED fitting ($12 M_\odot \text{ yr}^{-1}$ with BC03 models).

5. Photometric properties and SED fitting

5.1. Colors

The location of the selected galaxies in the $I - K_s$ vs. $K_s - m_{4.5}$ two-color plot is displayed in Fig. 6, showing that these

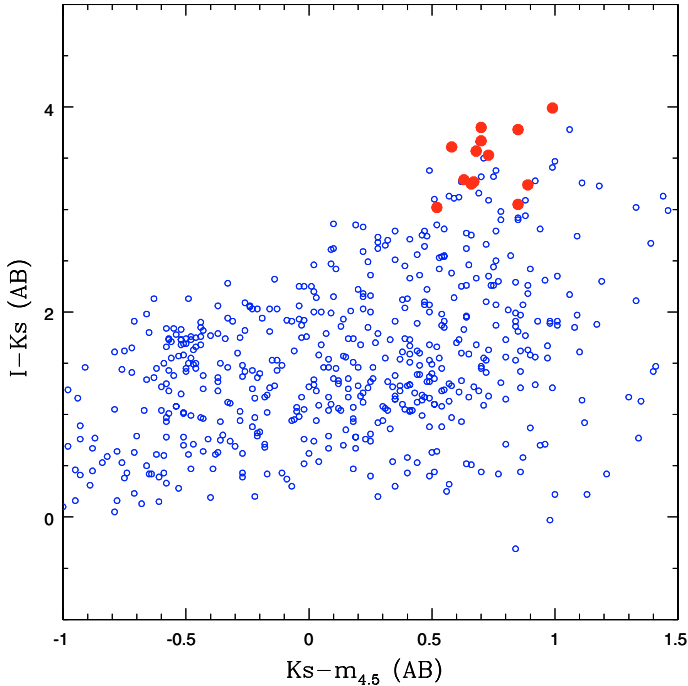


Fig. 6. The location of the selected passive galaxies (red filled circles) in the $I-K_s$ vs. $K_s-m_{4.5}$ diagram. Open blue symbols indicate GMASS galaxies with spectroscopic redshifts.

passive galaxies are among the reddest in both colors if compared to the GMASS galaxies with spectroscopic redshifts. In particular, their colors are all broadly consistent with the ones expected for passively evolving galaxies in the BzK diagram (Fig. 7) (Daddi et al. 2004b), especially when allowance is made for photometric errors. Note instead that these galaxies do not qualify as “Distant Red Galaxies” (DRGs, Franx et al. 2003), because they are all at $z < 2$, whereas the DRG selection criterion ($J - K_s > 2.3$ or $J - K_s > 1.37$ in Vega or AB system) is designed to select passive galaxies at $z > 2$. Indeed, the $J - K_s$ colors of our passive galaxies are all consistently $J - K_s \leq 1.37$ (actually, $0.7 < J - K_s \leq 1.37$).

5.2. SED fitting

As discussed in Sect. 3.2 and in previous studies (e.g. Cotter et al. 2006; Maraston et al. 2006), the rest-frame UV spectra are only sensitive to the most recent star formation events, whereas including in the analysis all the available photometric bands extending to the rest-frame near-IR should allow us to gather information also on the previous star formation history (SFH).

The photometric SED was derived for each of the 13 ETGs using the public images available in the GOODS-South field including 11 bands: optical (HST+ACS, $BVIz$; Giavalisco et al. 2004), near-infrared (ESO VLT+ISAAC, JHK_s) and mid-infrared (Spitzer+IRAC, $3.6 \mu\text{m}$, $4.5 \mu\text{m}$, $5.8 \mu\text{m}$, $8 \mu\text{m}$, Dickinson et al. in preparation).

We have used the synthetic spectra of M05 (Kroupa IMF) and BC03/CB07 (Chabrier IMF), adopting exponentially declining star formation histories $SFR = (M/\tau) \exp(-t/\tau)$ with $\tau = 0.1, 0.3, 1, 2, 3, 5, 10, 15$, and 30 Gyr, plus the case of constant star formation rate. For each value of τ , a set of synthetic SEDs is pre-calculated for ages (since the beginning of the model at $t = 0$) of 0.1, ..., 12 Gyr, in steps of 0.1, Gyr,

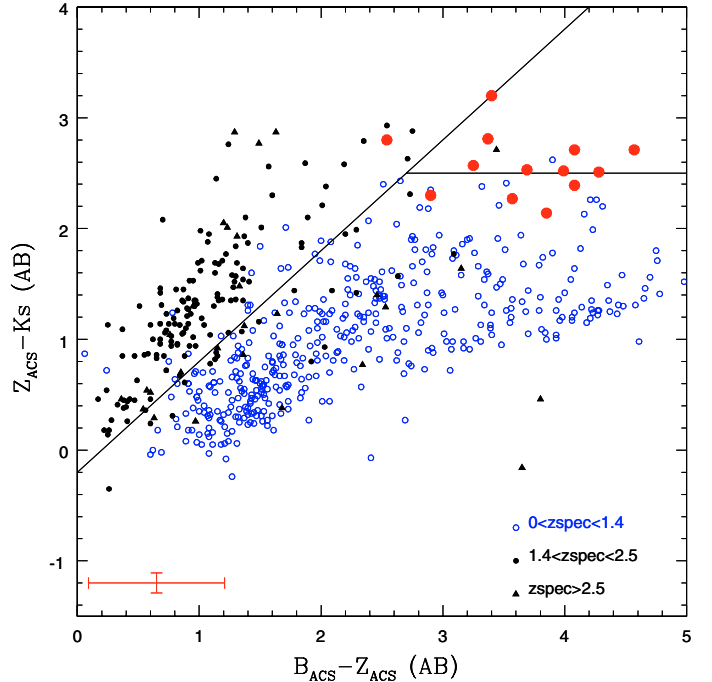


Fig. 7. The location of the selected passive galaxies (red filled circles) in the BzK color-color diagram (Daddi et al. 2004b). Blue open circles, black filled circles and triangles indicate GMASS galaxies with known spectroscopic redshifts $z < 1.4$, $1.4 \leq z \leq 2.5$ and $z > 2.5$ respectively. The red error bars in the bottom left corner indicate the average photometric uncertainty on the $z - K_s$ and $B - z$ colors for the selected passive galaxies. The errors on $B - z$ are very large due to the very faint B -band magnitudes.

and only τ -models with ages less than the age of the Universe at the redshift of each galaxy are retained in the best-fit procedure. Extinction has been treated as a free parameter in the optimization, having adopted the extinction curve of Calzetti et al. (2000). We have adopted solar metallicity for all the models. The fitting procedure selects the template spectrum that minimizes the χ^2 , and therefore gives a value for each of four parameters: the “age” of the best-fitting model, the e -folding time of the SFR τ , the extinction A_V , and the stellar mass. This latter quantity comes from the absolute normalization of the SED, once the best-fitting model has been chosen as the one providing the closest SED shape to the observed SED.

We caution that an exponentially declining SFR is certainly a convenient mathematical assumption, but the actual star formation history may be significantly different. At least for models with small τ values, the “age” given by the best-fitting procedure must be interpreted as *the age of the bulk stellar population of a galaxy*. Of course, real galaxies are likely to contain also stars significantly older than the “age” derived in this way. On the other hand, the best fit “age” derived from just the rest-frame UV spectrum (as in Sect. 3.2) corresponds to the age of the last significant episode of star formation.

During the fitting, only the observed bands corresponding up to the rest-frame K_s -band ($\lambda_{\text{rest}} < 2.5 \mu\text{m}$) were used in order to avoid any dust emission contamination. The redshifts are taken from the GMASS spectroscopy and are *not* free parameters, hence largely reducing the SED fitting degeneracies often occurring when also the (photometric) redshift is a free parameter. The absence of luminous AGN sources as inferred from the X-ray and $24 \mu\text{m}$ data (see previous Section) implies that the observed flux measured from the sample galaxies is dominated by

Table 3. Photometric SED fitting results ($Z = Z_{\odot}$).

ID	M_B	Age					Age					Age				
		BC03	A_V	M	SFR	τ	M05	A_V	M	SFR	τ	CB07	A_V	M	SFR	τ
472	-22.09	0.7	0.6	10.67	0.55	0.1	0.8	0.0	10.49	0.14	0.1	0.8	0.3	10.58	0.19	0.1
996	-20.42	1.3	0.6	10.30	0.01	0.1	0.8	0.6	10.16	0.07	0.1	1.3	0.0	10.03	0.01	0.1
1498	-21.88	1.6	0.6	10.89	2.07	0.3	0.7	0.4	10.61	0.45	0.1	2.0	0.0	10.77	0.43	0.3
2111	-21.80	2.3	0.1	10.86	0.20	0.3	1.1	0.0	10.61	0.01	0.1	1.1	0.1	10.56	0.01	0.1
2148	-22.52	1.3	0.4	11.04	0.01	0.1	1.3	0.2	11.02	0.01	0.1	2.8	0.0	11.19	0.09	0.3
2196	-22.15	1.3	0.3	10.84	0.00	0.1	1.3	0.0	10.79	0.00	0.1	1.1	0.1	10.68	0.01	0.1
2239	-21.40	1.3	0.5	10.64	0.00	0.1	1.1	0.2	10.54	0.01	0.1	1.0	0.5	10.56	0.02	0.1
2286	-21.39	2.0	0.5	10.80	0.47	0.3	1.1	0.2	10.56	0.01	0.1	2.3	0.1	10.71	0.14	0.3
2355	-21.62	0.8	0.6	10.54	0.17	0.1	0.9	0	10.36	0.04	0.1	0.8	0.4	10.44	0.14	0.1
2361	-21.85	2.8	0.2	11.04	0.07	0.3	1.4	0.2	10.83	0.00	0.1	3.0	0.0	10.99	0.03	0.3
2470	-22.07	2.2	0.1	10.94	0.33	0.3	1.1	0.0	10.71	0.01	0.1	1.0	0.3	10.73	0.03	0.1
2543	-21.30	1.1	1.8	11.00	12.4	0.3	1.0	0.6	10.69	0.03	0.1	2.1	0.6	10.88	0.40	0.3
2559	-22.09	2.2	0.1	10.95	0.34	0.3	1.0	0.0	10.67	0.03	0.1	1.1	0.0	10.63	0.01	0.1
Mean	-21.79	1.6	0.4	10.81	0.35	0.2	1.1	0.2	10.62	0.06	0.1	1.6	0.2	10.67	0.12	0.2
rms	0.53	± 0.6	± 0.2	± 0.22	± 0.57	± 0.1	± 0.2	± 0.2	± 0.28	± 0.12	± 0.0	± 0.8	± 0.2	± 0.28	± 0.15	± 0.1

Rest-frame absolute magnitudes (M_B) are relative to BC03 fitting. The three groups of columns (Age, A_V , M , SFR , τ) are relative to BC03, M05 and CB07 models respectively. The mean and rms of A_V and SFR for BC03 models are given excluding the highly discrepant values for object 2543. The units are Gyr, mag, $\log(M/M_{\odot})$, $M_{\odot} \text{ yr}^{-1}$ and Gyr for Age, A_V , Mass, SFR , τ respectively.

stellar radiation. We have also explored the effect of assuming other than solar metallicities, from sub-solar to super-solar. This was attempted only using the CB03/BC07 models, but the best fit was always achieved for solar metallicity. Table 3 shows the main results of SED fitting in the case of solar metallicity.

5.2.1. The stellar masses and their uncertainties

The procedure adopted here for measuring the stellar masses is basically the same as that generally followed in the literature (e.g. Fontana et al. 2004, 2006; Longhetti et al. 2005; Bundy et al. 2005, 2006; Pozzetti et al. 2007; Trujillo et al. 2007). While the details of our procedure are extensively discussed in Pozzetti et al. (2007), we recall here a few points. The internal accuracy of the measured stellar masses is ~ 0.2 dex, as derived from the width of the probability distributions in the fitting procedure. In addition to this typical internal error, systematic errors should also be mentioned. A first source of systematics is the choice of the IMF, which is not a free parameter in our procedure, but must be adopted a priori. Stellar masses derived assuming the Kroupa IMF are systematically higher by 0.04 dex than those derived assuming the Chabrier IMF, and this difference was subtracted from the masses derived with Maraston (2005) models (using Kroupa IMF), in order to allow a homogeneous comparison with the masses derived using the Bruzual & Charlot (2003) and the Charlot & Bruzual (2007) models. The use of a straight, single-slope Salpeter IMF would result in masses about 70% higher. Another source of uncertainty is the assumption made on the star formation history. For instance, detailed simulations (e.g. Fontana et al. 2004; Pozzetti et al. 2007) showed that in the case of an underlying exponentially declining SFH with $SFR \propto \exp(-t/\tau)$ plus random bursts of star formation superimposed on it, the estimated stellar masses become higher by $\approx 30\text{--}40\%$. Finally, as mentioned above the stellar population models differ in their treatment of the TP-AGB phase of evolution, which is particularly important for stellar populations in the age range 0.5–2 Gyr, and most of the galaxies in the present study fall in this range of ages. As already pointed out by Maraston et al. (2006) and Wuyts et al. (2007), BC03 models give stellar masses that are systematically larger by $\approx 40\text{--}60\%$ than those estimated

with M05 models (see Fig. 8). This is most likely due to the best fitting algorithm boosting the mass in order to compensate for the lacking TP-AGB contribution in the BC03 models. The stellar masses from CB07 and M05 models are instead in fairly good agreement. It is important to remind that similar uncertainties on photometric stellar masses are also present in the SED fitting of low- z SDSS galaxies (see Kauffmann et al. 2003). However, we also recall that the stellar masses are generally in good agreement with the dynamical masses, especially for early-type galaxies (see e.g. Drory et al. 2004; di Serego Alighieri et al. 2005; Rettura et al. 2006).

The stellar masses (and luminosities) of our sample galaxies span a rather wide range of values, from very massive and luminous (like the high- z ETGs discussed in Cimatti et al. 2004; McCarthy et al. 2004), to a regime of lower luminosity and stellar masses that was possible to reach thanks to the deep GMSS spectroscopy ($-20.4 < M_B < -22.5$, $10.0 < \log(M/M_{\odot}) < 11$).

5.2.2. The age of the dominant stellar population

In the case of M05 models the ages of the dominant stellar populations are remarkably homogeneous around ~ 1 Gyr, with a small scatter of ± 0.2 Gyr (Table 3). The best fit is always achieved with the smallest e -folding time, i.e., $\tau = 0.1$ Gyr. Being $\langle z \rangle = 1.6$ for these galaxies, this age estimate implies that the bulk of the stellar populations should have formed at $z = 2\text{--}2.5$. The same procedure applied to BC03 and CB07 models gives a somewhat older average age, ~ 1.6 Gyr, implying a peak formation redshift $\sim 2.5\text{--}3$. However, in this case there appears to be a much larger age dispersion (± 0.8 Gyr), with some ages being as high as ~ 3 Gyr, corresponding to a peak formation redshift ~ 5 . In general, for these older galaxies the e -folding time indicated by CB07 models is longer, and the stellar mass somewhat higher than indicated by M05 models. This discrepancy suggests that the two sets of models are still appreciably different, most likely in the way the TP-AGB phase is implemented, as it is clearly shown in Fig. 5.

We note that for all galaxies when using M05 models, and for most using the CB07 ones, the SED ages derived in this

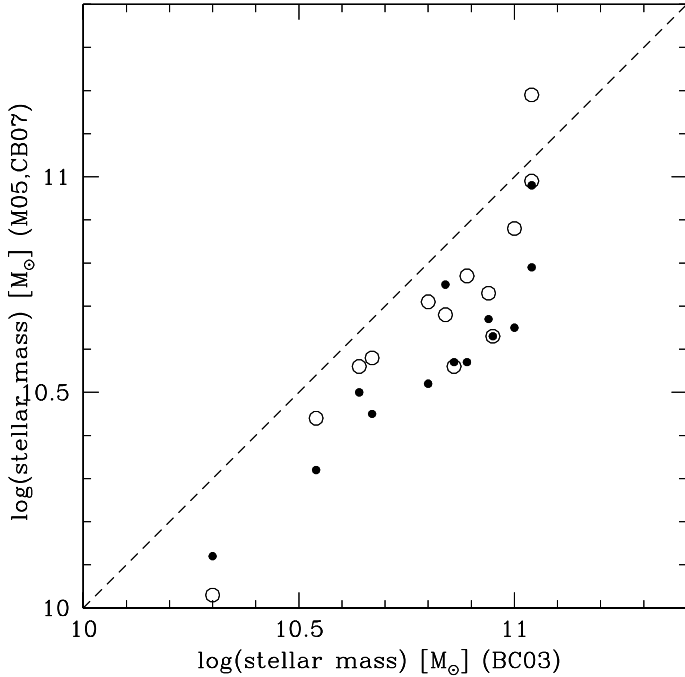


Fig. 8. Comparison between stellar masses derived with Bruzual & Charlot (2003), Maraston (2005) (filled circles) and Charlot & Bruzual (2007) (open circles) synthetic spectral templates.

section are very much consistent with that derived solely from the rest-frame, stacked UV spectrum in Sect. 3, i.e. ~ 1 Gyr. We interpret this agreement as an additional indication that most of the star formation activity was confined within a short time interval, short compared to the typical age (~ 1 Gyr) of the stellar populations. In this respect, we also note that in spite of τ models having been widely used in the literature, nature may have proceeded differently: rather than starting abruptly at its maximum intensity and then declining exponentially, star formation is likely to have started at low level at very high redshift, then increasing exponentially as mass is accumulated with $\dot{M} \propto M$ (Daddi et al. 2007a), and finally suddenly truncated by feedback effects. If so, an *inverted* τ model would be more appropriate.

We can conclude that, by and large, our analysis indicates that the bulk of stars in these passively evolving galaxies must have formed at $z \approx 2-3$, a result in excellent agreement with the evidence for ETGs from $z = 0$ to $z \approx 1$ (as extensively reviewed in Renzini 2006), as well as for other $z > 1.4$ ETGs (Cimatti et al. 2004; McCarthy et al. 2004; Daddi et al. 2005a; Saracco et al. 2005; Longhetti et al. 2005; Kriek et al. 2006).

5.2.3. Extinction and star formation rates

By giving an age and an e -folding time, the best fitting procedure automatically implies an ongoing SFR for each galaxy. Note however that the procedure is not specifically optimized to estimate this quantity, and therefore the results should be regarded only as rough estimates or upper limits. Nevertheless, these *implied* SFR s are typically very low, especially in the case of M05 models, as indeed expected for passive galaxies. For two galaxies (ID 1498 and 2543) BC03/CB07 models give substantially higher SFR s than for all other galaxies, and one of them (ID 2543) is the one with the strongest [OII] $\lambda 3727$ flux and the only one marginally detected at $24 \mu\text{m}$.

Even assuming the SFR s in Table 3 at face value, the implied specific star formation rates are very low (i.e. star

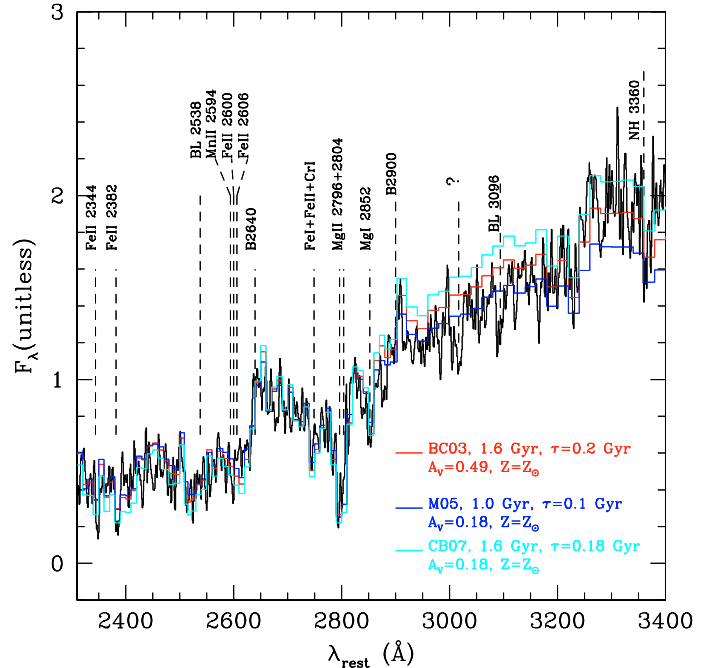


Fig. 9. Comparison between the average spectrum of GMASS passive galaxies and the three synthetic spectral templates corresponding to the average best fit results of the photometric SED fitting. The spectral resolution of the templates is lower than in the stacked spectrum.

formation rate per unit mass, $SSFR = SFR/M$), as shown in Fig. 10. These $SSFR$ s are typical of the lower envelope of the $SSFR$ distribution at $1 < z < 2$ characteristic of the general population of the oldest galaxies with just residual, if any star formation (Feulner et al. 2005; Juneau et al. 2005; Kriek et al. 2006). This implies that our sample galaxies cannot increase their stellar mass significantly at the current rate of star formation. For instance, they cannot double their mass from the look-back time of their redshifts to the present day. The inverse of the $SSFR$ represents the characteristic secular timescale of the stellar mass growth. For our sample galaxies, these timescales are in the range of $30-10^4$ Gyr.

The dust extinction inferred from the SED fitting analysis is generally very low (with some exceptions with BC03 model fitting). By forcing $A_V = 0$ the results of the SED fitting do not change substantially: the median age increases by a factor of 2 for BC03 and $< 25\%$ for both M05 and CB07, τ slightly increases by 20% and 5% for BC03 and CB07 respectively, whereas no significant changes occur for the stellar masses (5% for BC03 and $< 2\%$ for M05 and CB07). The test with $A_V = 0$ indicate that the results of the SED fitting are stable (especially for M05 and CB07 models) and that the major source of uncertainty remains the choice of the synthetic spectra library.

The properties inferred with SED fitting are in broad agreement with the characteristics of the UV spectra, as shown in Fig. 9 where the stacked spectrum of the passive galaxies is compared with the three synthetic spectral templates corresponding to the average best fit results of the photometric SED fitting (see Table 3).

6. Morphological properties

6.1. The HST data

Thanks to the availability of deep and ultra-deep HST imaging from GOODS and HUDF projects, it was possible to

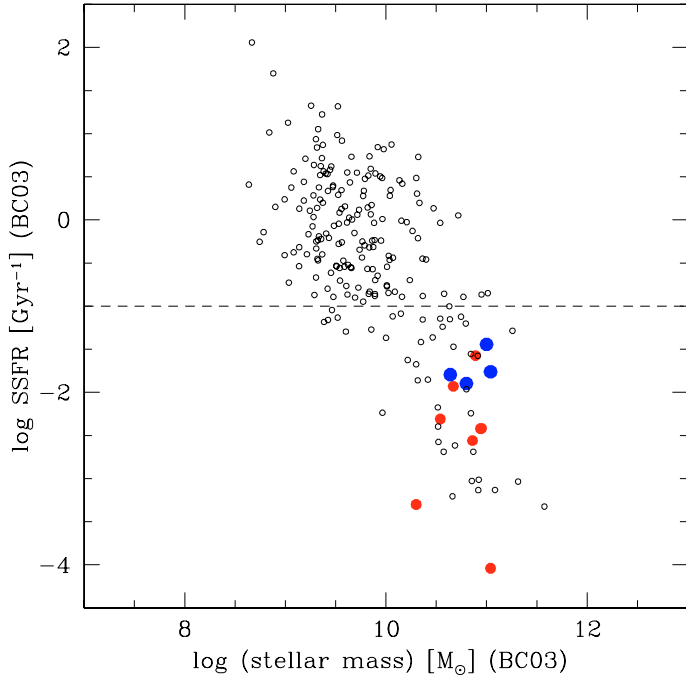


Fig. 10. The *SSFRs* of galaxies with star formation activity detected in the spectra or inferred from the photometric SED fitting. The blue circles indicate the four galaxies with observed $[\text{OII}]\lambda 3727$ emission. The red circles show the galaxies for which the formal *SFR* comes from the photometric SED fitting (with BC03 models). With M05 or CB07 models, the *SSFRs* are even smaller or close to $SSFR \sim 0$. Black circles indicate the general distribution of galaxies in the same redshift range of our sample ($1.3 \leq z < 2$) using the data of Feulner et al. (2005). The dashed line indicates the *SSFR* required to double a galaxy’s mass between the average redshift in this $1.3 \leq z < 2$ bin and the present (assuming a constant *SFR*).

complement the spectroscopy and photometry with quantitative morphological information. GOODS has surveyed the Chandra Deep Field South (CDFs) with ACS and filters $F435W$ (B), $F606W$ (V), $F775W$ (I) and $F850LP$ (z), with exposure times respectively of 3, 2.5, 2.5 and 5 orbits. HUDF has instead surveyed a smaller area of about 3×3 arcmin² which has a large overlap with the GMASS field (see Kurk et al. 2007a, for further details) in the same 4 bands, but with exposure times respectively of 56, 56, 150 and 150 orbits. For both datasets the publicly available images were drizzled to a scale of 0.03 arcsec/pixel in order to improve the PSF pixel sampling. Furthermore, the HUDF was observed also with deep NICMOS imaging of 2.5×2.5 arcmin² with $F110W$ and $F160W$ filters (Thompson et al. 2005). NICMOS images were drizzled to a final scale of 0.09 arcsec/pixel.

6.2. Visual classification

A visual classification based on eye inspection was performed on the whole GMASS sample independently by two of us (PC and GR). The global morphological results will be presented in a forthcoming paper (Cassata et al. 2007, in preparation). The visual analysis was always done in the ACS filter band closest to the rest-frame B -band. For the objects at $z > 1$ (like the ones presented in this paper), the analysis was done in the reddest filter available (z -band). The classification scheme is based on 6 classes (see also Cassata et al. 2005): 1. ellipticals/S0 galaxies; 2. peculiar ETGs (i.e. ETGs with signs of interaction or with

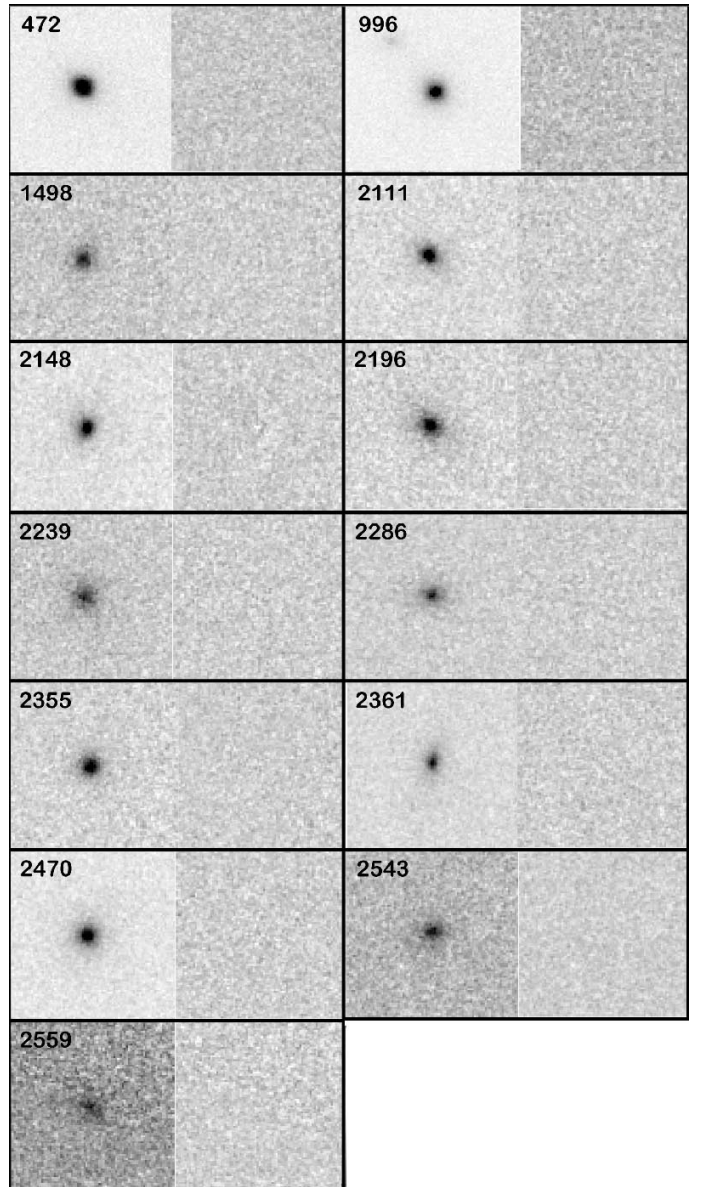


Fig. 11. Gallery of the 13 passive galaxies in the sample. Each postage stamp is 2.4×2.4 arcsec². On the right of each galaxy cutout, the images of the GALFIT residuals are also shown.

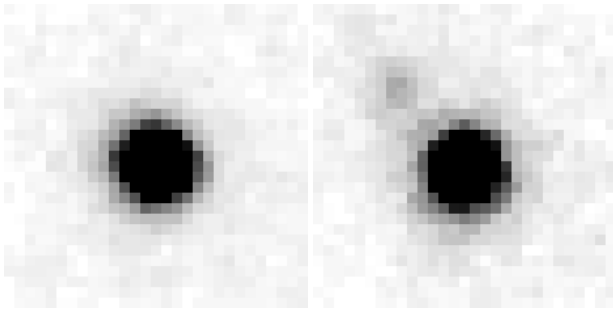
some isophotal asymmetry); 3. normal spirals; 4. perturbed spirals, that is disk galaxies with an evident bulge but showing also asymmetries due to interactions or regions of enhanced star formation; 5. irregular galaxies; 6. compact objects. In Fig. 11 we present a gallery of the 13 galaxies in the sample. Each box is 2.4×2.4 arcsec², corresponding to about 20 kpc at redshift 1.5.

Figure 11 clearly shows that the majority of passive galaxies have the spheroidal morphology characteristic of ETGs. In particular, we classified 7 of them as pure ellipticals, as they appear resolved, concentrated and very regular; 2 of them have been classified as spirals (2239 and 2559), as they are not very concentrated; finally; 4 have been placed in the compact class, i.e. with very concentrated and regular morphological structure (472, 2286, 2361 and 2543) (see Table 4). The NICMOS + $F160W$ images available in the HUDF for the galaxies IDs 472 and 996 show very compact and spheroidal morphologies at $\lambda_{\text{rest}} \approx 0.5\text{--}0.6$ μm (Fig. 12).

Table 4. Surface brightness fitting results (ACS F850LP band).

ID	Class	n	r_e arcsec	R_e kpc	μ_e mag arcsec ⁻²
472	6	4.1 ± 0.7	0.076	0.64 ± 0.13	15.52 ± 0.43
996	1	4.6 ± 0.7	0.100	0.84 ± 0.17	17.78 ± 0.43
1498	1	1.5 ± 0.2	0.120	1.01 ± 0.20	16.71 ± 0.43
2111	1	4.0 ± 0.4	0.099	0.84 ± 0.17	16.39 ± 0.43
2148	1	3.7 ± 0.3	0.142	1.20 ± 0.24	16.45 ± 0.43
2196	1	6.0 ± 0.9	0.380	3.22 ± 1.22	18.95 ± 0.82
2239	4	2.2 ± 0.2	0.256	2.16 ± 0.43	18.84 ± 0.43
2286	6	2.6 ± 0.3	0.159	1.35 ± 0.27	17.82 ± 0.43
2355	1	2.2 ± 0.2	0.096	0.81 ± 0.16	16.48 ± 0.43
2361	6	4.1 ± 0.4	0.133	1.13 ± 0.23	16.97 ± 0.43
2470	1	4.2 ± 0.3	0.215	1.81 ± 0.36	17.78 ± 0.43
2543	6	2.2 ± 0.3	0.167	1.41 ± 0.28	18.02 ± 0.43
2559	4	1.0 ± 0.5	0.171	1.43 ± 0.29	17.25 ± 0.43

Class: visual classification (Sect. 6.2).

**Fig. 12.** NICMOS images (2.4×2.4 arcsec²) of IDs 472 and 996.

6.3. Surface brightness profile analysis

We used GALFIT (Peng et al. 2002) to model the surface brightness distribution for the galaxies in our sample. As these galaxies are very red and become rapidly very faint going to short wavelengths, GALFIT was run on the image taken with the reddest available ACS filter (z -band, filter *F850LP*). The PSF with which GALFIT convolves the models during the fit process was obtained by averaging 10 stars in the field. Two of the objects (472 and 996) lie in HUDF area, so they have been analyzed in the HUDF ACS F850LP image, while the other 11 have been analyzed in GOODS image. We also attempted to analyze galaxies IDs 472 and 996 in the HUDF NICMOS + *F160W* image, but the fitting did not provide stable and reliable results due to their small sizes with respect to the pixel scale and the difficulty to derive the PSF because of the very few suitable stars available.

In all cases, we used a Sérsic profile to model the galaxy surface brightness profiles:

$$I(r) = I_e \exp \left\{ -b_n \left[\left(\frac{r}{r_e} \right)^{1/n} - 1 \right] \right\} \quad (1)$$

where $I(r)$ is the surface brightness measured at distance r , I_e is the surface brightness measured at the effective radius r_e and b_n is a parameter related to the sersic index n . For $n = 1$ and $n = 4$ the Sérsic profile reduces respectively to an exponential or deVaucouleurs profile. Bulge dominated objects having typically high n values (e.g. $n > 2$) and disk dominated objects having n around unity.

6.4. Simulations

To test the capability of GALFIT to obtain reliable size measurements we made use of simulations. To this purpose, we built a set of galaxies with a wide range of properties, to take into account all possible systematic biases. In particular, we have chosen a grid of values for magnitudes, radii, Sérsic indices and axial ratios. Apparent magnitudes m_z span from 22.5 to 24.5, reflecting the magnitude distribution of the 13 real galaxies in the sample. The range of radii goes from 0.06 to 0.45 arcsec (basically from 2 pixels to the typical size that local galaxies with masses comparable to those of our sample would have at $z \sim 1.4-2$). Sérsic indices n span from 1 to 6 and axial ratios b/a varied between 0.4 and 1. A set of 1000 galaxies was built by randomly selecting the above parameters from their intervals. Then, the galaxies were simulated using GALFIT, and convolved with the same average star PSF used for the fitting process. Finally, the simulated galaxies were placed in the real z -band ACS/GOODS-South image in random positions in order to take into account possible systematics due to deblending and variations of the local background. The same GALFIT fitting process used for the 13 real galaxies was then applied to derive the morphological parameters of the simulated galaxies. First, we used *SExtractor* to obtain first estimates for magnitude, size, axial ratio and orientation. Second, we ran GALFIT using the *SExtractor* values as first guesses. In the fitting procedure, $n_{\text{Sérsic}}$ was left free to vary between 0.5 and 8. The noise images requested by GALFIT to estimate χ^2 , were built using proper values of RMS, GAIN and EXPTIME.

The results of this process are summarized in Fig. 13, where we show the fractional error on the measured size as a function of the output size. This allows a simple comparison between the sizes and errors estimated with this technique for our 13 real galaxies and the results of simulations. It can be noted that for small sizes the average error is very close to zero, with a small scatter. For large sizes, instead, the error distribution moves towards positive values, and the scatter increases. This tendency to overestimate sizes for large objects is also dependent on the magnitude, being mild for galaxies with $m_z < 23.75$ and more important for object with $m_z > 23.75$. In any case, this overestimate is relevant only for objects with sizes larger than 0.25–0.3 arcsec. In the same figure, we also show the radii measured for the 13 galaxies in the sample, together with the formal errors determined by GALFIT. It can be seen that 4 and 9 of them are respectively brighter and fainter than $m = 23.75$, and that 12 have measured sizes smaller than ~ 0.25 arcsec, in the regime where the simulations show no systematic errors and a small scatter. Only one object has a measured size larger than 0.3 arcsec, for which the simulation shows a typical overestimate of the size of about 20%. The size for this object can thus be considered as an upper limit.

Overall, the errors measured by GALFIT are smaller than the scatter shown by simulated galaxies with similar output sizes. Most of the 13 galaxies have sizes for which the simulation shows a scatter of about 20%, so we decided to assign a minimum fiducial error of 20% to our galaxy sizes.

6.5. GALFIT results

Once assessed the capability of GALFIT of retrieving robust measurements of the size even for galaxies at high redshift, we run the code on our 13 galaxies, using *SExtractor* estimates of magnitude, size, axial ratio and position angle as first guesses. The GALFIT results are shown in Table 6. The residual maps provided by GALFIT, as result of the subtraction of the best fit

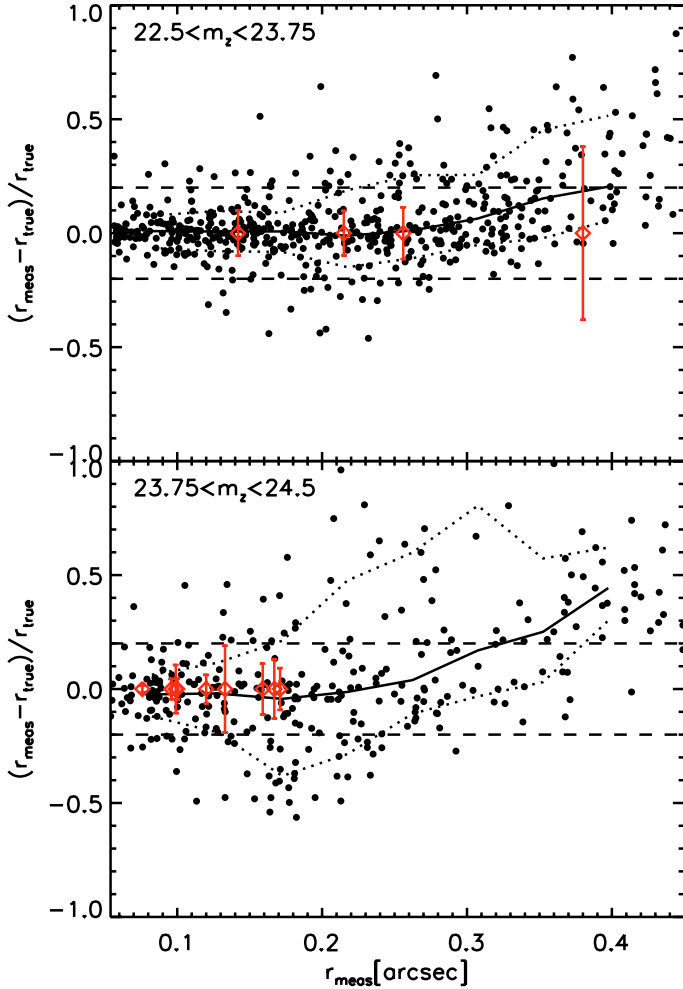


Fig. 13. The fractional difference between measured (r_{meas}) and input (r_{true}) sizes for the 1000 simulated galaxies, as a function of the output size. The upper and the lower panel show the results for galaxies brighter and fainter than $m_z = 23.75$ respectively. The solid line shows the median of the error distribution, and the dotted lines includes 68% of the objects. The dashed lines indicate the limiting regions relative to errors of $\pm 20\%$. Red symbols show the measured sizes for the 13 galaxies in the sample, together with the formal error measured by GALFIT.

model from the original galaxies, show no significant structures for all the galaxies (Fig. 11). 11 of the 13 objects have best fit solutions with Sersic index $n > 2$, indicating that the bulk of the galaxy light comes from a dominant bulge component (e.g. in Fig. 14). In our sample, among the 7 galaxies visually classified as pure ellipticals, 6 have $n \sim 4$. In the class of visually classified ellipticals, only galaxies 1498, 2355 and 2559 are best fitted by a smaller value of the Sersic index ($n \sim 1-2$). The GALFIT results broadly agree with what was anticipated by the visual classification, i.e. that passive galaxies at $z \sim 1.4-2$ have the typical morphology of ETGs, as in the present-day Universe.

The galaxy angular sizes were circularized as $r_e = a_e(1 - \epsilon)^{1/2}$, where a_e and ϵ are the effective radius along the major axis and the ellipticity of the galaxy morphology respectively. The values are in the range of 0.07–0.38 arcsec, corresponding to 0.6–3.2 kpc (Table 4). Of the two galaxies located in the HUDF (IDs 472 and 996) previously identified by Daddi et al. (2005a) (IDs are 3650 and 8238 respectively), ID 472 has n and r_e consistent within the errors with those of Daddi et al. (2005), whereas

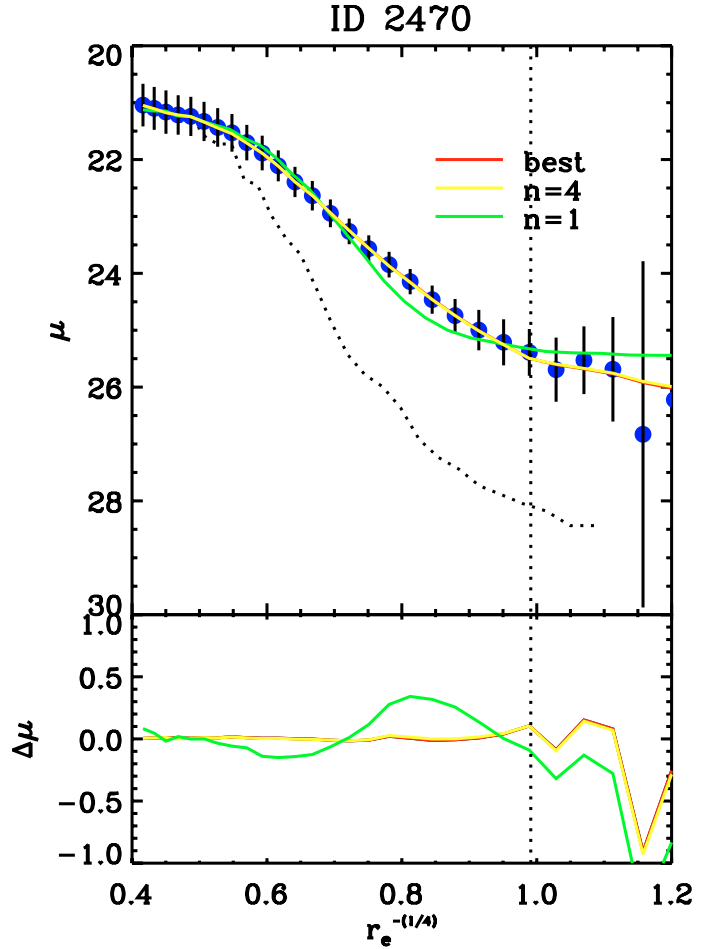


Fig. 14. Example of an ACS z -band surface brightness profile fit expressed in mag arcsec^{-2} (μ) relative to the galaxy ID 2470 where a $r^{1/4}$ profile provides a very good match with the data (with r expressed in arcsec). The black dotted, red, yellow and green lines indicate respectively the PSF profile, the formal best fit profile, the profile for $n = 4$ (de Vaucouleurs) and the profile for $n = 1$ (exponential). The bottom panel shows the residuals between the best fit curves and the observed profile.

for ID 996 we measure a significantly smaller r_e . Here we adopt our measurements for ID 996.

In our morphological analysis, the reddest filter available for all galaxies (ACS F850LP), does not cover the rest-frame optical, but the rest-frame mid-UV ($\approx 3000-4000 \text{ \AA}$, i.e. approximately the U -band). This might introduce a bias due to the possible morphological K -correction and/or the internal color gradients usually present in ETGs, thus resulting in a wavelength-dependent size of the galaxies. In particular, gradients with colors redder towards the center (as often observed in ETGs; e.g. Peletier et al. 1990) could make the sizes measured in the optical larger than those in the UV. However, McIntosh et al. (2005) showed that for this kind of gradient, the expected size variation from the rest-frame U -band to the R -band is $\Delta r/r_{\text{obs}} \approx -0.075(z - 0.47)$. This means that our galaxies would have sizes larger by only $\approx 6-11\%$ if observed in the rest-frame R -band for the redshift range of our sample ($1.4 < z < 2$). Other results indicate that the sizes of spheroidal galaxies do not change substantially as a function of wavelength (e.g. by comparing r_e measured in ACS and NICMOS bands; e.g. see McGrath et al. 2007a; Trujillo et al. 2007).

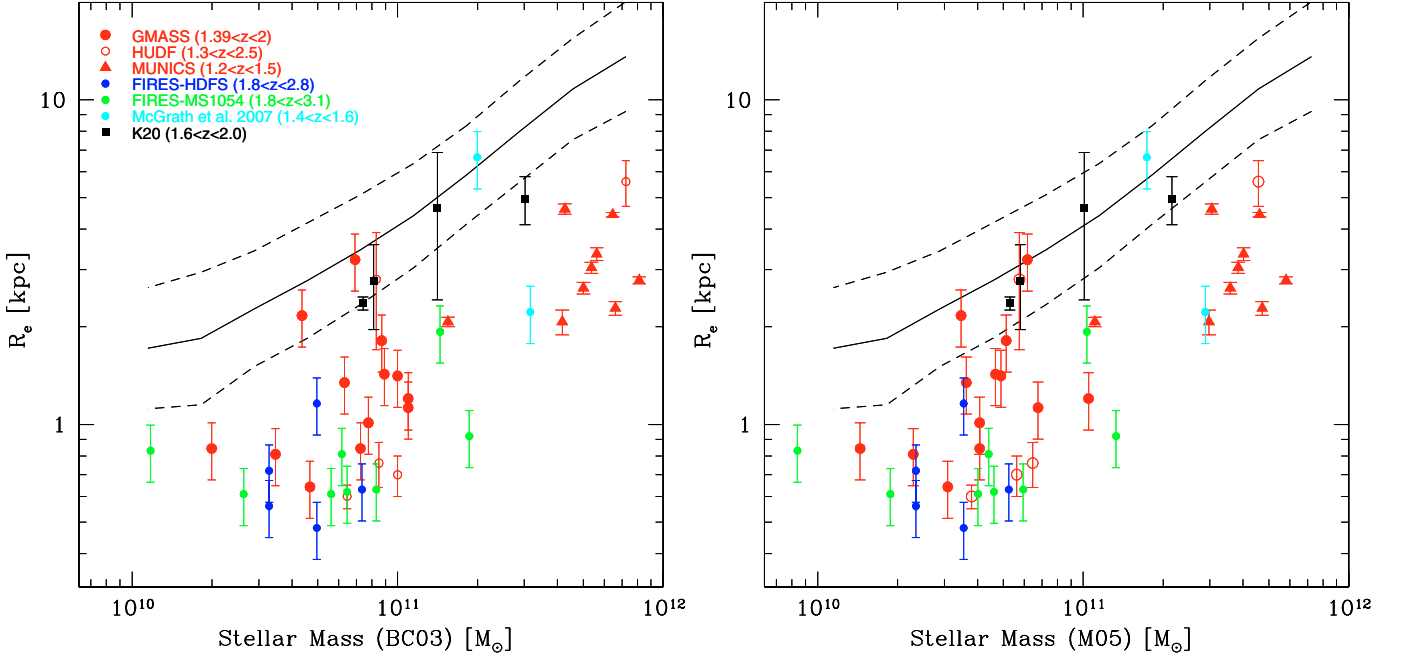


Fig. 15. The distribution of physical sizes versus stellar mass for passive galaxies in the GMASS sample (red filled circles). For clarity, error bars are not shown. Stellar masses are estimated with BC03 (*left panel*) and M05 (*right panel*) spectral synthesis models. The solid line shows the local size-mass relation of ETGs as derived with the SDSS sample by Shen et al. (2003), with the dashed lines indicating the $\pm 1\sigma$ scatter around this relation. Blue, green, cyan filled circles indicate the passive galaxies of Zirm et al. (2007) (FIRES – HDFS), Toft et al. (2007) (FIRES – MS1054) and McGrath et al. (2007b) respectively, the red triangles show the MUNICS massive galaxies of Trujillo et al. (2006) and Longhetti et al. (2007), the red open circles show the HUDF passive galaxies of Daddi et al. (2005) and Maraston et al. (2006), the black filled squares the K20 galaxies of Cimatti et al. (2004). The two galaxies of McGrath et al. (2007b) whose SEDs were fitted with CB07 templates are located in the right panel.

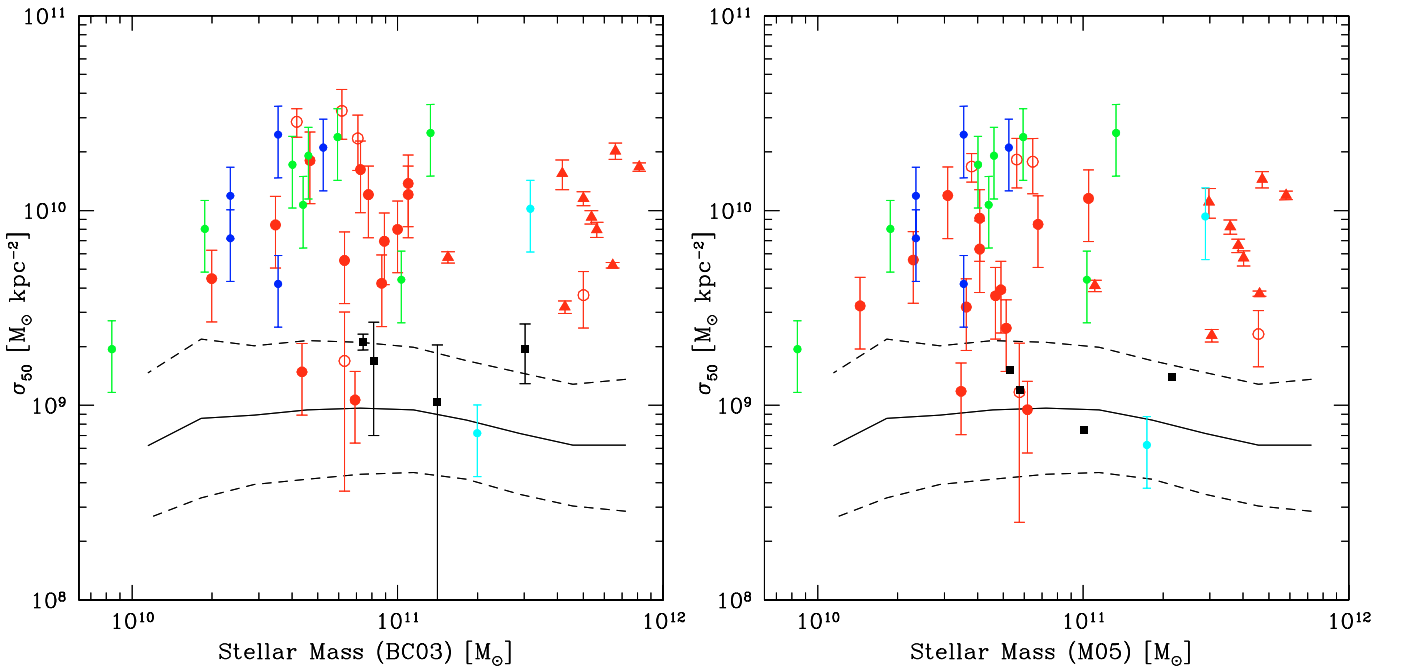


Fig. 16. The distribution of stellar mass surface density (σ_{50}) versus stellar mass for passive galaxies. The symbols are the same of Fig. 15. The solid line shows the local size-mass relation from the SDSS sample by Shen et al. (2003), with the dashed lines indicating the scatter around this relation.

As discussed in the next sections and found in other works (e.g. Daddi et al. 2005a; Trujillo et al. 2006), the sizes derived for most of our sample galaxies are much smaller than the ones observed at $z \sim 0$ in ETGs with the same stellar mass. We explored the possibility that these small r_e may be partly due to the presence of a point-like unresolved central source which

dominate the surface brightness profiles and bias the estimate of r_e towards small values. Thus, we attempted to perform fits with a two-component surface brightness profile made by a central unresolved source (using the stellar PSF) plus a Sersic profile. In all cases we found no significant improvements in the resulting best fit profile with respect to those obtained with a single

(Sersic) component. More importantly, we found that typically less than 16% of the light (corresponding to $\Delta\text{mag} > 2$) is located in the putative central component, and the estimated values of r_e are all consistent with the ones obtained with the single component fitting within 10%. This experiment strengthens even more that the r_e measured for most galaxies in our sample are reliable and indeed very small.

7. The size-mass relation

Early-type galaxies at $0 < z < 1$ follow a well-defined size-mass relation (e.g. Shen et al. 2003; McIntosh et al. 2005), with the size increasing as a function of mass. Models of galaxy formation predict different size-mass relations depending on the history of mass assembly (see Shen et al. 2003).

The role of GMASS is the secure spectroscopic identification of a significant number of passive galaxies down to lower masses than in previous samples at $1.4 < z < 2$ which were biased towards the most massive systems (e.g. Daddi et al. 2005a; Trujillo et al. 2006; McGrath et al. 2007a; Trujillo et al. 2007). This allows us to better probe the size-mass relation of ETGs at $z \approx 1.4$ – 2 down to $\approx 10^{10} M_\odot$.

The size – stellar mass relation for the passive galaxies in our sample is presented in Fig. 15 and compared with the local size-mass relation measured by Shen et al. (2003) for ETGs in the SDSS and with other passive galaxies at $z > 1.2$ from the literature. We note that in the local relation published by Shen et al. (2003, their Table 1) there was a typo in the b parameter, while here we used the correct one ($b = 2.88 \times 10^{-6}$; Shen, private communication).

In the comparison amongst different samples, it is important to account for the differences in the adopted synthetic stellar population models and IMFs. Throughout the present work, we adopt a Chabrier IMF and scale all the literature masses to that IMF with the following relations: $\log M(\text{Chabrier}) = \log M(\text{Salpeter}) - 0.23$ and $\log M(\text{Chabrier}) = \log M(\text{Kroupa}) - 0.04$. In addition to the IMF conversion, it is sometimes necessary to scale stellar masses by taking into account the different model spectra used to fit the SEDs. Based on previous (e.g. Wuyts et al. 2007; Maraston et al. 2006) and present results (Sect. 5.2), we adopted the conversion $\log M(\text{M05}) = \log M(\text{BC03}) - 0.15$ in order to take into account the average decrease (≈ 40 – 50%) of M05 masses with respect to BC03 results for galaxies at $z \approx 1$ – 3 .

Shen et al. (2003) adopted a Kroupa IMF and used the stellar masses that were previously estimated by Kauffmann et al. (2003) through the comparison of observed features in the SDSS spectra with BC03 template spectra. However, we decided not to scale the local size-mass relation of Shen et al. (2003) to account for the difference between BC03 and M05 masses because at $z \sim 0$ the typical ages of ETGs are so old (several Gyr) that the effects of TP-AGB stars should be negligible. For the sample of Daddi et al. (2005a) we used the most recent SED fitting results of Maraston et al. (2006) who adopted a Kroupa IMF and provided stellar masses estimated with both BC03 and M05 models. Trujillo et al. (2006) adopted a Kroupa IMF and their stellar masses refer to BC03 models. For the sizes of the MUNICS galaxies, we adopted those of Longhetti et al. (2007). For the FIRES sample galaxies, Zirm et al. (2007) used M05 models and a Salpeter (1955) IMF, whereas Toft et al. (2007) used BC03 models and a Salpeter IMF. We recall that the redshifts of the FIRES galaxies of Zirm et al. (2007) and Toft et al. (2007) are photometric. We also added two spheroidal galaxies

at $z \sim 1.5$ selected from the sample of McGrath et al. (2007a,b) who adopted BC03 (with Chabrier IMF) for their SED fitting.

Figure 15 shows that passive galaxies at $z > 1.2$ follow a clear size-mass relation. However, the majority of them has sizes significantly smaller than at $z \approx 0$ for a fixed stellar mass, whereas only 15–20% are located within the scatter region of the $z \sim 0$ relation of Shen et al. (2003).

The result on the small sizes at $z > 1.2$ holds independently of the adopted stellar masses (cf. Fig. 15 left and right panels). For the GMASS galaxies only (for which we also have stellar masses estimated with CB07 models), the results are very similar to those of M05 stellar masses if CB07 stellar masses are used. The average ratio between the observed sizes and the size at $z \sim 0$ (Shen et al. 2003) for the same stellar mass (all scaled to BC03 + Chabrier IMF) is $\langle R_e(z)/R_e(0) \rangle = 0.42 \pm 0.25$ and 0.29 ± 0.14 for $1 < z < 2$ ($\langle z \rangle = 1.60$) and $2 < z < 4$ ($\langle z \rangle = 2.52$) respectively. No significant correlation was found between the galaxy size R_e (or $\langle R_e(z)/R_e(0) \rangle$) and physical or environmental properties (age of the stellar population, SFR , $SSFR$, rest-frame colors, A_V , location inside our outside the structure at $z = 1.61$).

The sizes smaller by a factor of ≈ 2 – 3 than at $z \sim 0$ imply that the stellar mass surface densities are ≈ 5 – 10 times larger. Figure 16 shows the stellar mass surface densities (σ_{50}) of the passive galaxies as a function of stellar mass and the comparison with the $z \approx 0$ relation derived from Shen et al. (2003) sample. The stellar mass surface densities are estimated as $\sigma_{50} = 0.5M/\pi R_e^2$. The difference with respect to $z \sim 0$ galaxies becomes even more striking if stellar volume densities are considered: an excess by a factor of 3 in size (R_e) corresponds to a factor of ≈ 30 in volume density.

8. Comparison with early-type galaxies at $z \approx 1$

We also explored how the picture changes at lower redshifts using the small, but highly complete spectroscopic sample of K20 Survey (Cimatti et al. 2002b) ETGs at $0.8 < z < 1.3$ for which also the absorption line velocity dispersion (σ_V) is available. Figure 17 shows that at $z \sim 1$ more galaxies can be located within the $z \sim 0$ relations (see also McIntosh et al. 2005; Trujillo et al. 2007).

From the scaling relation of ETGs (e.g. Jorgensen et al. 1995; van Dokkum van Dokkum 2005), it is expected that the densest systems should have necessarily the highest velocity dispersion. Figure 17 shows that while ETGs with high σ_V are located both inside and outside the R_e -mass relation at $z \approx 0$, most of the smallest/densest outliers have high values of σ_V . The migration of passive galaxies in the R_e - M and σ_{50} - M planes from regions of small size and high density to the $z \approx 0$ relations (Figs. 15–17) is further evidence that the redshift range of about $1 < z < 2$ is the critical cosmic epoch for the assembly and structural transformation of ETGs (e.g. Fontana et al. 2004; Glazebrook et al. 2004; Abraham et al. 2007; Arnouts et al. 2007).

9. The Kormendy relation

In the absence of the velocity dispersion measurements needed to study where the GMASS passive galaxies lie in the Fundamental Plane of ETGs, we explored how they behave with respect to the Kormendy relation, i.e. a projection of the Fundamental Plane which correlates μ , the mean surface brightness within r_e and the physical size R_e .

This relation for our sample is shown in Fig. 18. The B -band rest-frame magnitude is measured during the photometric SED

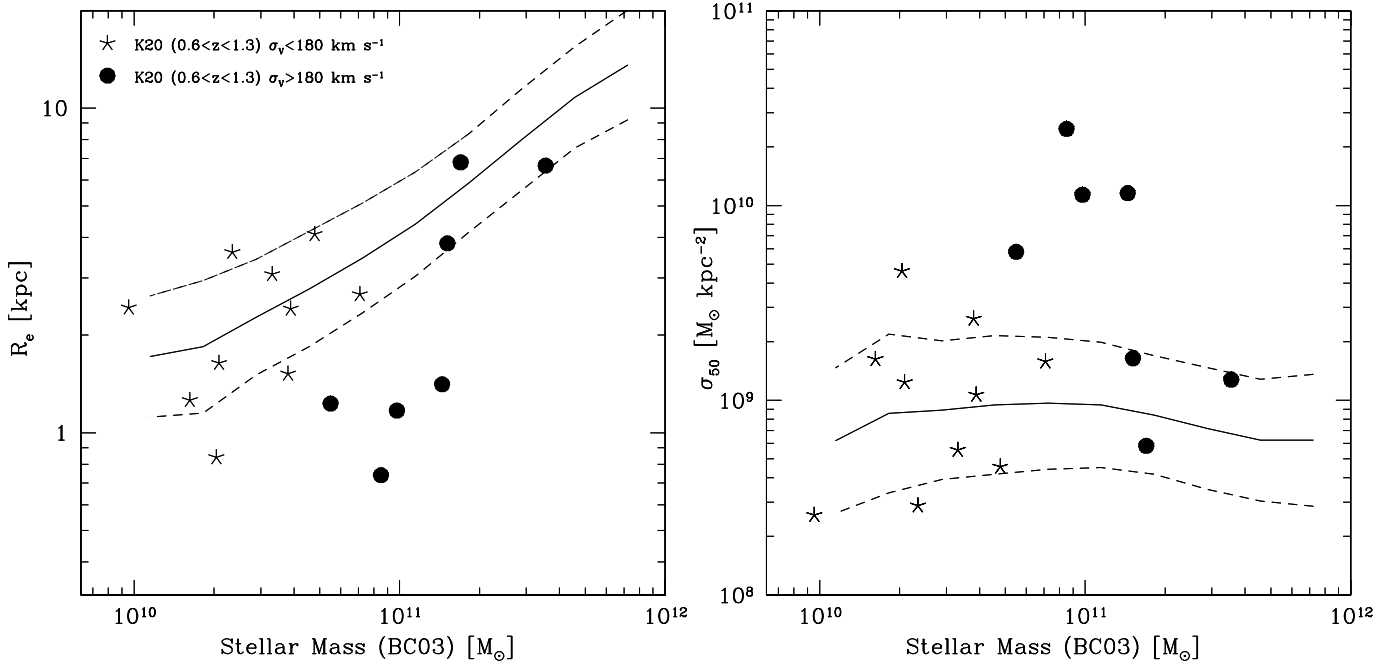


Fig. 17. *Left panel:* the distribution of physical sizes versus stellar mass for ETGs at $z \approx 1$. The solid line shows the local size-mass relation of ETGs as derived with the SDSS sample by Shen et al. (2003), with the dashed lines indicating the scatter around this relation. The starred and filled symbols indicate the K20 ETGs from di Serego Alighieri et al. (2005) with velocity dispersion $\sigma_v < 180 \text{ km s}^{-1}$ and $\sigma_v > 180 \text{ km s}^{-1}$ respectively. *Right panel:* the distribution of stellar mass surface density (σ_{50}). The symbols are the same of left panel.

fitting process described in Sect. 5.2. Here we applied the appropriate correction for the surface brightness dimming effect. The mean surface brightness μ_B is finally computed as:

$$\mu_B = M_B + DM(z) + 2.5 \log(2\pi) + 5 \log(r_e) + 10 \log(1+z), \quad (2)$$

where M_B is the absolute magnitude in the B -band, $DM(z)$ is the distance modulus at redshift z , r_e is the effective radius in arcsec and z is the redshift of the galaxy.

As a local ($z \sim 0$) reference, we took the Kormendy relation for Coma galaxies by Jorgensen et al. (1995). In Fig. 18 we show both the individual Coma galaxies and the best fit to their relation together with its $\pm 1\sigma$ scatter. We also plot the $z \sim 1.4$ galaxies of Longhetti et al. (2007): their measurements (done on NICMOS images and then converted into the rest-frame Gunn r band) have been properly translated in B -band magnitudes applying a typical color $B-r = 1.4$, and appear to be in good agreement with ours. It can be noted that the Kormendy relation seems to evolve very strongly between $z \sim 0$ and $z \sim 1.5$. In particular, galaxies of the same size appear to be more luminous by an amount between 2 and 3 mag. This brightening is dependent on the physical size, being larger for smaller galaxies, thus making the slope of the relation steeper at $z \sim 1.5$. In any case, all the galaxies, if they have to end on top of the local relation, must fade their luminosity by more than 2 mag from $z \sim 1.5$ to $z \sim 0$. This fading exceeds by at least 0.5 mag the largest possible fading predicted by spectral evolution models of passive red galaxies (see also Longhetti et al. 2007, for a similar result). Since the surface mass density drops by a factor of 5–10 in the same redshift range, it means that these high- z compact and dense galaxies can reach the local Kormendy relation only through a combination of increase in size (R_e) and fading due to the passive evolution of the stellar populations.

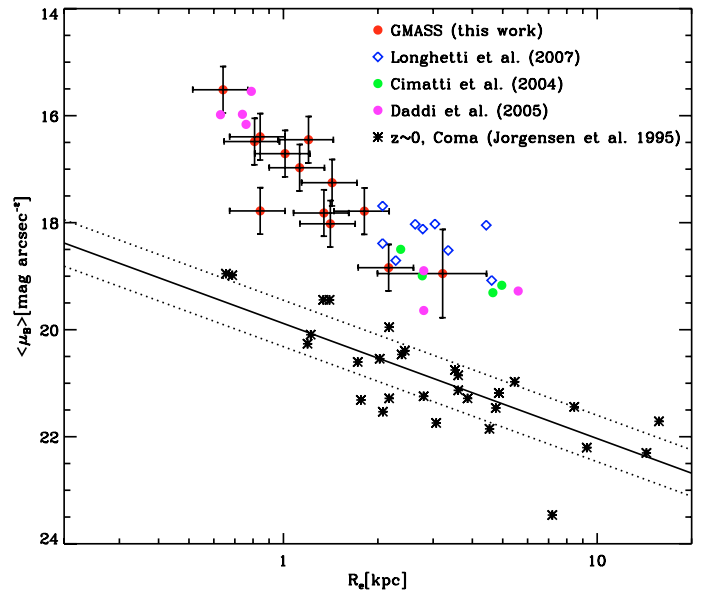


Fig. 18. Mean surface brightness within r_e in the B -band against R_e for our sample (red filled circles). Coma elliptical galaxies are shown as stars, together with their best fit (solid line) and biweight scatter. Open blue lozenges show $z \sim 1.4$ galaxies from Longhetti et al. (2007).

10. Are there superdense relics at $z \approx 0$?

The superdense ETGs identified at $z > 1$ seem to disappear in the present-day Universe (e.g. Shen et al. 2003). However, recent works based on SDSS data showed that there is a population of very massive ETGs with $\sigma_v > 350 \text{ km s}^{-1}$ which, compared to ETGs of the same luminosity, are characterized by very small sizes (Bernardi et al. 2006, 2007). Thus, we investigated whether some of these local galaxies have properties similar to those observed in passive galaxies at $z > 1$.

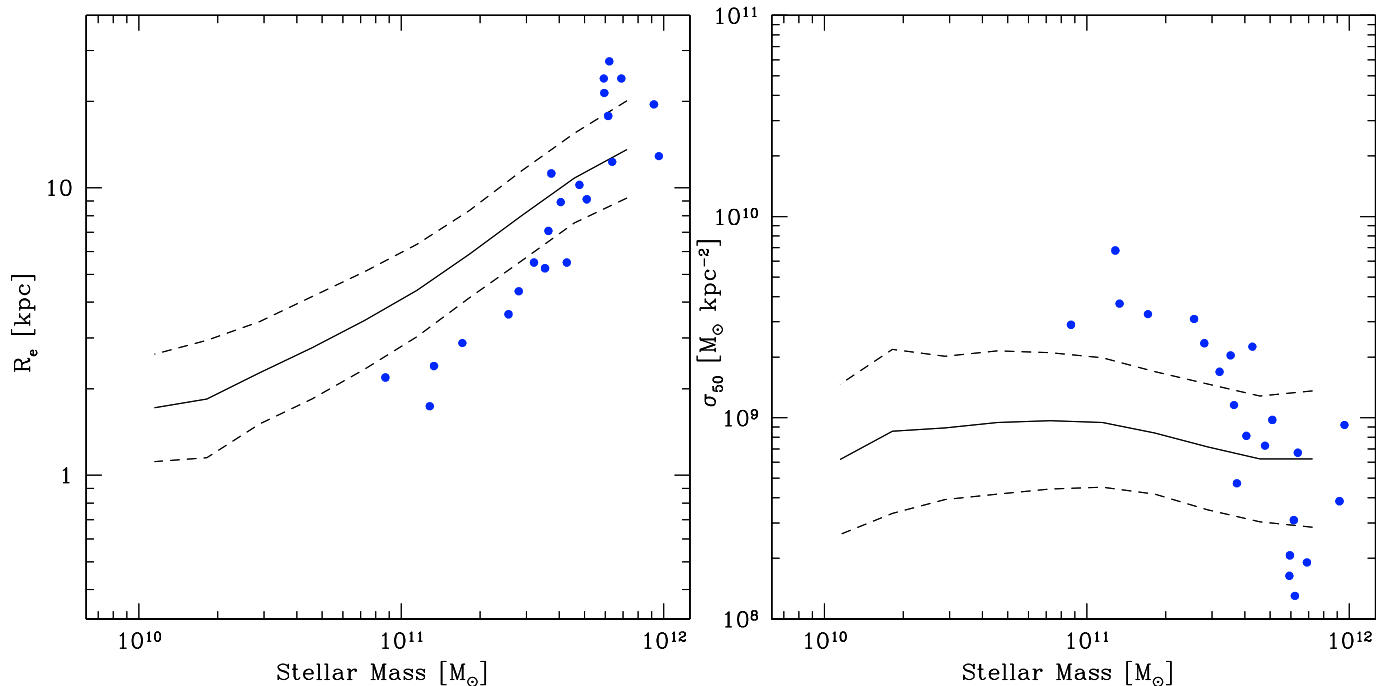


Fig. 19. The location of the ETGs at $z \approx 0$ with $\sigma_v > 350 \text{ km s}^{-1}$ identified by Bernardi et al. (2006); Bernardi et al. (2007) in the SDSS sample (blue circles) compared to the global relations of Shen et al. (2003) (same as in Figs. 15–17).

Figure 19 shows the location of these galaxies in the R_e -mass and σ_{50} -mass planes. The stellar masses derived with the method described by Kauffmann et al. (2003; that are also used by Shen et al. 2003) were associated to the ETGs in the sample of Bernardi et al. (2007; Brinchmann, private communication). Figure 19 shows that there are a few outliers which are not located within the Shen et al. (2003) relations and are characterized by small sizes around 1–2 kpc with stellar masses around $10^{11} M_\odot$. These systems show a significant excess in stellar mass surface density σ_{50} (Fig. 19), but never as strong as observed in ETGs at $z > 1$. The number density of these systems at $z \sim 0$ is very small ($\approx 10^{-7}$ – 10^{-8} Mpc^{-3} , Bernardi et al. 2006), and much smaller than the characteristic abundance of passive galaxies at $1 < z < 2$ ($\approx 10^{-4} \text{ Mpc}^{-3}$, Kong et al. 2006). Thus, we conclude that superdense relics with $R_e \approx 1 \text{ kpc}$ at $z \approx 0$ are extremely rare with respect to $z > 1$, and absent if $R_e < 1 \text{ kpc}$. However, in the “smooth envelope accretion” scenario discussed in Sect. 11.2.2, it might be possible that the superdense galaxies observed at $z \approx 1.5$ survived as hidden, very dense cores inside present-day ETGs.

11. New constraints and open questions

These findings provide new pieces in the puzzle of massive galaxy formation and evolution, but at the same time open new crucial questions: (1) how did these systems form? (2) What mechanism(s) can explain their subsequent size growth and decrease of the internal density?

11.1. How did the superdense galaxies form?

The mere existence of $\approx 1 \text{ Gyr}$ old, passively evolving galaxies up to $z \approx 2$ implies that the bulk of stars formed at higher redshifts. In particular, the constraints on the age, τ and stellar masses indicate that the star formation at $z > 2$ – 2.5 was very intense (e.g. $SFR > 100 M_\odot \text{ yr}^{-1}$) in order to form stellar

mass up to $M \geq 10^{11} M_\odot$ with such short timescales (see also Cimatti et al. 2004; McCarthy et al. 2004; Daddi et al. 2005a; Saracco et al. 2005; Longhetti et al. 2005; Kriek et al. 2006).

The small sizes and high internal mass densities of the passive galaxies at $1 < z < 2$ provide new observational clues which help to unveil the nature of their precursors. Amongst all the precursor candidates mentioned in the Introduction, only the submm/mm-selected galaxies (SMGs) (Blain et al. 2002) have sizes and mass surface density comparable to those of passive galaxies (Tacconi et al. 2006, 2007).

Table 5 compares the properties of SMGs and passive galaxies. The similarity between the properties of the two populations is striking, with the notable exception of the comoving number density, with SMGs being an order of magnitude rarer (comoving number density $\approx 10^{-5} \text{ Mpc}^{-3}$; Scott et al. 2002; Chapman et al. 2005) than the passive descendants ($\approx 10^{-4} \text{ Mpc}^{-3}$; Daddi et al. 2004b; Daddi et al. 2005a; Kong et al. 2006).

The other populations of massive star-forming galaxies identified at $z \gtrsim 1.5$ – 2 (e.g. *BzK*, *BM/BX*, ...) show distinct properties if compared to SMGs: much larger sizes in the range of 2–8 kpc and mass surface densities lower by an order of magnitude ($\approx 10^{2-3} M_\odot \text{ pc}^{-2}$) (see Bouché et al. 2007).

The difference in these properties may reflect distinct dynamical and assembly histories. SMGs may represent the cases where rapid and highly dissipative major mergers occur at $z > 2$ with timescales of $\approx 0.1 \text{ Gyr}$ (e.g. Narayanan et al. 2006; Khochfar & Silk 2006a; Tacconi et al. 2006, 2007, and references therein) and leave very compact, superdense remnants which then evolve almost passively at $1 < z < 2$ (see also Swinbank et al. 2006). The other star-forming systems selected in the optical and near-infrared at $z > 2$ may have a less violent evolution characterized by star formation activity extended over longer timescales (≈ 0.5 – 1 Gyr , Daddi et al. 2005b) and by multiple minor mergers or rapid dissipative collapse from the halo, with either process capable to form early disks. These massive

Table 5. Comparison between passive galaxies and SMGs.

	Quiescent galaxies	SMGs
Redshift	$z \approx 1.5$	$z \approx 2.5$
Age of the Universe	4.3 Gyr	2.7 Gyr
Mass	$10^{10-11} M_{\odot}$ (stars)	$10^{10-11} M_{\odot}$ (gas)
Size	1–2 kpc (stars)	1–2 kpc (gas)
Mass surface density	$10^{3-4} M_{\odot} \text{pc}^{-2}$ (stars)	$10^{3-4} M_{\odot} \text{pc}^{-2}$ (total)
Starburst timescale	0.1–0.3 Gyr	≈ 0.1 Gyr
Star formation rate	$< 1 M_{\odot} \text{yr}^{-1}$	$\approx 100\text{--}1000 M_{\odot} \text{yr}^{-1}$
Number density	$\approx 10^{-4} \text{Mpc}^{-3}$	$\approx 10^{-5} \text{Mpc}^{-3}$
Correlation length	$r_0 \approx 8\text{--}10 \text{Mpc}$	$r_0 \approx 6.9 \pm 2.5 \text{Mpc}$

disks may later also evolve into spheroids through disk instabilities of further merging processes (see Genzel et al. 2006).

In this framework, objects like GMASS ID 2543 might represent the transition phase of an object with a substantially developed old stellar population concentrated in a bulge-like structure which dominates the spectrum, SED and morphology, but with still a residual star formation activity of a few solar masses per year as indicated by the weak [O II] $\lambda 3727$ emission and the possible detection at $24 \mu\text{m}$.

Under the assumption that all passive galaxies at $z \approx 1.5$ are the descendants of the starburst phase occurring in SMGs at $z \approx 2.5$, the characteristic timescale (“duty cycle” or the “duration”) of the SMG phase can be estimated as the ratio of the comoving number densities of the two populations and the amount of cosmic time available from $z \approx 2.5$ to $z \approx 1.5$ (≈ 1.5 Gyr), i.e. ≈ 0.15 Gyr. This timescale is broadly consistent with the e -folding timescale derived independently from the SED fitting and from the recent studies based on SMG molecular gas (Tacconi et al. 2006, 2007).

The evolutionary link between rapid, dissipational, gas-rich merging or collapse (traced observationally by the SMG phase) at $z \approx 2\text{--}3$ and the superdense passive spheroids at $z \approx 1\text{--}2$ provides one of the strongest constraints known to date on the physical mechanisms capable to lead to the formation of massive spheroidal galaxies. Although the physical processes are completely different, this mechanism is somehow reminiscent of the “old-fashioned” monolithic collapse.

11.2. How did the superdense galaxies disappear?

The other major question is to understand how the superdense galaxies decreased their internal stellar mass density from $z \approx 1.5\text{--}2$ and migrated to the local size-mass relation at $z \approx 0$.

11.2.1. Dissipationless merging

One possibility is the dissipationless (“dry”) major merging of ETGs. According to some models (Nipoti et al. 2003a; Nipoti et al. 2003b; Dominguez-Tenreiro et al. 2006; Naab et al. 2007; Ciotti et al. 2007; Boylan-Kolchin et al. 2006), this process can increase the final size and mass of the system without altering substantially the stellar population content. In particular, Boylan-Kolchin et al. (2006) found that, under a set of orbital requirements, the stellar remnants of major dry mergers lie on the Fundamental Plane of their progenitors, and that the increase of the size with the increasing stellar mass is expected to follow a relation $R_e \propto M^{\alpha}$, with $0.6 \leq \alpha \leq 1.3$ depending on the orbital properties (see also Nipoti et al. 2003b; Ciotti et al. 2007).

Figure 20 shows the expected growth of R_e as a function of mass for the extreme values of α , and suggests that $\alpha \gtrsim 1$ is

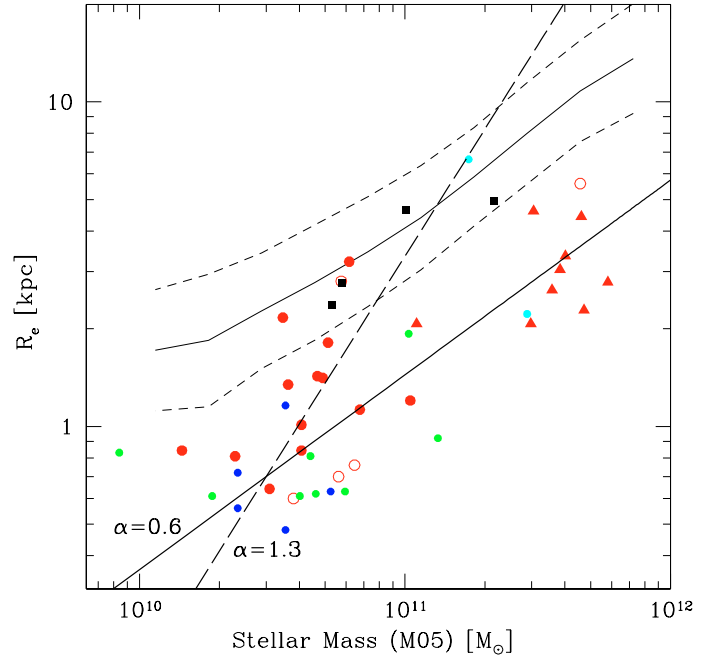


Fig. 20. The size-mass relation of passive galaxies at $z > 1.3$. The symbols are the same of Fig. 15. Stellar masses are estimated with M05 spectral synthesis models. The thin solid line shows the local size-mass relation of ETGs as derived with the SDSS sample by Shen et al. (2003), with the thin dashed lines indicating the $\pm 1\sigma$ scatter around this relation. The thick solid and long-dashed lines indicate the expected increase of the size due to dissipationless merging with $R_e \propto M^{\alpha}$, with $\alpha = 0.6$ and $\alpha = 1.3$ respectively, and normalized to $R_e = 0.7$ kpc and a stellar mass of $3 \times 10^{10} M_{\odot}$.

needed to grow efficiently the compact galaxies from $z \approx 1.5$ and move them onto the local size-mass relation at $z \approx 0$. However, given all possible orbital parameters in dry merging events, we may expect the *effective* value of α to be appreciably lower than its maximum value. Therefore, the ability of dry merging alone to solve the problem remains questionable.

The dry merging hypothesis can in principle be tested by deriving the statistics of pairs of close/interacting passive galaxies as a function of redshift. The redshift range $1 < z < 2$ seems to be the most important one because of the substantial decrease of the superdense ETG fraction from $z \approx 1.4\text{--}2$ to $z \approx 0.6\text{--}1.3$ (Fig. 17 vs. Fig. 15; see also McIntosh et al. 2005; Trujillo et al. 2007). Unfortunately, no dry merger statistics is available in this redshift range (see e.g. Bell et al. 2006). We also recall that to be fully valid, the dry merging scenario should also be consistent with the recent findings of a very weak evolution of the stellar or dynamical mass functions of luminous and massive ($> 10^{11} M_{\odot}$) ETGs at $z \leq 0.7\text{--}0.8$ (e.g. Bundy et al. 2007; Bundy et al. 2006; Borch et al. 2006; Cimatti et al. 2006; Scarlata et al. 2006; Pozzetti et al. 2007).

Due to the limited statistics of the present GMASS sample, it is not possible to place any strong constraint on the dry merging scenario. However, we note that 12 out of 13 galaxies (see Fig. 11) have no visible companions within a distance of about 10–15 kpc. The only exception is represented by ID 996 which has a companion galaxy located at a small distance, but neither spectroscopic nor photometric redshift are available for this galaxy. The only available constraint comes from the color ($F110W - F160W \approx 0.6$) which looks similar to that of ID 996 ($F110W - F160W \approx 0.8$). However, even if this galaxy is at the same redshift of ID 996 and it will merge with it, this would

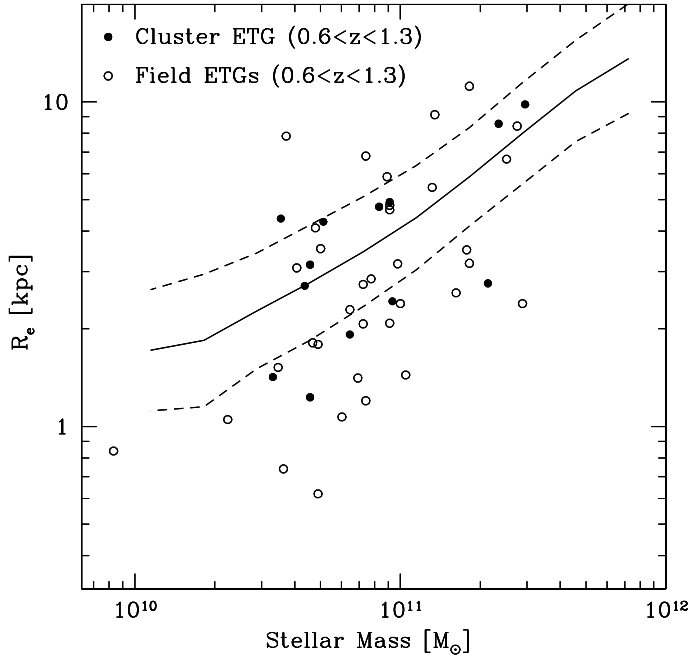


Fig. 21. The distribution of physical sizes versus stellar mass for ETGs at $z \approx 1$ of Rettura et al. (2006). The solid line shows the local size-mass relation of ETGs (Shen et al. 2003), with the dashed lines indicating the scatter around this relation. The filled and open symbols indicate cluster and field ETGs respectively. Stellar masses are homogeneously estimated with the PEGASE model spectra (Kroupa IMF).

not represent a “major” merger as the companion is fainter than ID 996 by ≈ 2.5 mag, corresponding to a luminosity (or \approx mass) ratio of $\approx 1:10$.

Even if clear cases of dry merger candidates are not present in our sample, we note that about half of the passive galaxies found in the GMASS spectroscopic sample lie in the dense structure at $z = 1.61$ (Vanzella et al. 2006; Castellano et al. 2007; Kurk et al. 2007b). The 7 galaxies present in this redshift spike have typical angular separations among themselves of ≈ 10 arcsec, corresponding to ≈ 85 kpc. It is tempting to speculate that some of these galaxies will later merge with each other along the filaments of this structure and form one or more larger massive ETG at lower redshift (see e.g. Nipoti et al. 2003b). McCarthy et al. (2007) have recently identified a compact cluster or group of red (passive) galaxies at $z = 1.5$ which may represent an example of a short-lived phase leading to the subsequent assembly of more massive ETGs at later cosmic times.

In this framework, further constraints can come from the differential evolution of the size-mass relation of ETGs as a function of the environment. We preliminarily investigated this issue using the sample of Rettura et al. (2006) which includes literature cluster and field ETGs at $z \approx 0.6$ – 1.3 . The sample is small and by no means complete. However, Fig. 21 suggests that environmental effects might be an important component of the size-mass relation evolution. Cluster ETGs seem to be preferentially located within or closer to the size-mass relation at $z \approx 0$ with respect to the ETGs located in low density environment. If confirmed with larger and complete samples, this may be consistent with the scenario where the mass assembly and size growth of ETGs is accelerated within high-density environment.

Recent simulations attempted to explain the size evolution of ETGs in the scenario of dissipationless merging. Khochfar & Silk (2006b) used semianalytical models to show that the size of elliptical galaxies (relative to $z \approx 0$) depends on the available

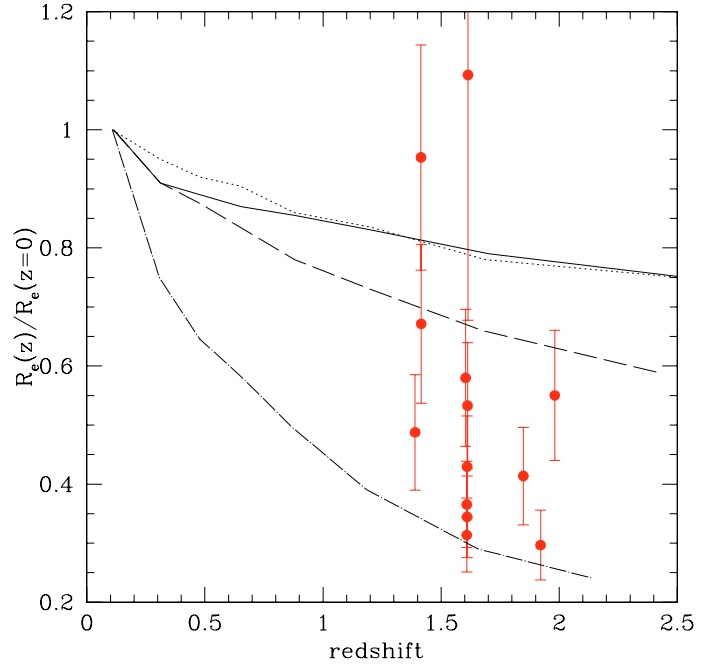


Fig. 22. The ratio of R_e of GMASS passive galaxies to the mean size of $z \approx 0$ ETGs, $\langle R_e(z, \mathcal{M})/R_e(0, \mathcal{M}) \rangle$, as derived from Shen et al. (2003). M05 stellar masses are used here. The curves represent the predictions of the Khochfar & Silk (2006b) model relative to the *final masses* at $z = 0$. Solid, dotted, dashed, dotted-dashed lines are relative respectively to the following ranges of stellar masses at $z \approx 0$: $1 \times 10^{10} < \mathcal{M}(z = 0) < 5 \times 10^{10} M_\odot$, $5 \times 10^{10} < \mathcal{M}(z = 0) < 1 \times 10^{11} M_\odot$, $1 \times 10^{11} < \mathcal{M}(z = 0) < 5 \times 10^{11} M_\odot$, $5 \times 10^{11} < \mathcal{M}(z = 0) < 1 \times 10^{12} M_\odot$.

amount of cold gas and the fraction of stars formed during the major merger event with which these galaxies formed. In this scenario, massive galaxies formed at high redshifts through gas-rich mergers which produced elliptical “remnants” characterized by small sizes. The size evolution is stronger for more massive galaxies as they involve more gas at high redshifts when they form, compared to less massive ellipticals, and galaxies of the same mass at low redshift form mostly from gas-poor mergers (see also Khochfar & Silk 2006a). According to this picture, local ellipticals with *present-day* stellar masses $10^{10} < \mathcal{M}(z = 0) < 10^{11} M_\odot$ were only ≈ 1.25 times smaller at $z = 2$, whereas those with $\mathcal{M}(z = 0) > 5 \times 10^{11} M_\odot$ were ≈ 4 times smaller at $z = 2$. Khochfar & Silk (2006b) also predict that the most massive ellipticals undergo on average 1–2 substantial “dry” mergers between $z = 2$ and today.

Figure 22 shows the location of the GMASS passive galaxies with respect to the model predictions of Khochfar & Silk (2006b). The ratio $R_e(z)/R_e(z = 0)$ was obtained dividing the observed effective radius of the GMASS galaxies by that at $z = 0$ derived from the stellar mass-size relation of SDSS ETGs of Shen et al. (2003) at the same mass of the GMASS passive galaxies. M05 stellar masses are used in this comparison, but the results do not change significantly if BC03 or CB07 masses are used. According to this comparison, the model predictions suggest that most GMASS passive galaxies are the progenitors (or the high- z counterparts) of ETGs that *today* have stellar masses of $10^{11} < \mathcal{M}(z = 0) < 10^{12} M_\odot$, i.e. they are the progenitors of the most massive E/S0 systems at $z \approx 0$.

11.2.2. Smooth envelope accretion

With an alternative approach based on smoothed particle hydrodynamics (SPH) simulations, Naab et al. (2007) showed that ETGs can be formed with appropriate cosmological initial conditions and even without requiring recent major merger events or feedback from supernovae or AGN. These models also predict small sizes around 1–2 kpc at $z > 1$. The Naab et al. (2007) approach is also relevant because it shows that during the early formation at $z > 2$ the assembly of massive ellipticals is dominated by mergers of gas-rich subcomponents and in situ star formation in a way characteristic of a dissipative collapse. Thereafter, smooth stellar accretion or minor/major mergers become more important and tend to dominate at $z < 1$, although major mergers are not always necessarily needed. In these simulations, the size evolution is mostly driven by the *accreted stars*. While the half-mass radius of the stars formed in situ (at high redshifts) remains almost constant independent of redshift, the accreted stars form an *envelope* whose half-mass radius increases smoothly with decreasing redshift around the compact and dense “seed” formed at higher redshifts. If this scenario is correct, we may expect to find the compact, superdense cores “hidden” inside present-day ETGs.

12. Summary and outlook

We presented a study of a 4.5 μm -selected sample of passive galaxies spectroscopically identified at $z \approx 1.4$ –2 with the GMASS survey (Kurk et al. 2007a). This work benefits from ultra-deep VLT+FOR2 optical spectroscopy complemented with multi-band photometry (0.4–8 μm) and HST imaging to investigate the physical, structural and evolutionary properties of these galaxies. The main results can be summarized as follows.

- The GMASS passive galaxies have spectra and SEDs dominated by old stars and very weak or absent star formation. A comparison of the stacked rest-frame UV spectrum (equivalent to an integration time of ~ 500 h) with three different libraries of stellar population model spectra indicates an age of ≈ 0.7 –2.8 Gyr for a metallicity range of 1.5–0.2 Z_{\odot} . Extending the model fitting at longer wavelengths using near-infrared and IRAC photometry helps to reduce the age-metallicity degeneracy and indicates ages of ≈ 1 –1.6 Gyr, $Z = Z_{\odot}$, e -folding timescales $\tau \sim 0.1$ –0.3 Gyr, where $SFR(t) \propto \exp(-t/\tau)$, and very low dust extinction. A comparison of the two libraries of model spectra which include TP-AGB stars shows that for a fixed age of 1 Gyr, the Maraston (2005) templates show a better agreement with the photometry than those of Charlot & Bruzual (2007) available to date.
- Neither individual galaxies nor their stacked images are detected in the X-rays with *Chandra* data. This implies that a luminous AGN source ($L_X > 10^{42}$ erg/s) is absent or is very heavily obscured. However, the possibility of dust obscuration seems unlikely because none of the galaxies has been detected at 24 μm , with only one marginal exception of one galaxy at $z = 1.61$.
- The stellar masses, estimated through the photometric SED fitting, are in the range of $10^{10-11} M_{\odot}$ and the specific star formation rates are very low ($\lesssim 3 \times 10^{-2}$ Gyr $^{-1}$). The stellar masses estimated with model spectra including TP-AGB stars are systematically lower by 0.1–0.2 dex than those estimated with models which do not include this phase of stellar evolution.
- The HST+ACS morphological and surface brightness profile analysis indicate that the majority of the spectroscopically-selected passive galaxies have spheroidal morphologies consistent with being analogous to present-day ETGs. However, their sizes are smaller by a factor of ≈ 2 –3 than at $z \approx 0$, and imply that the stellar mass surface and volume internal densities are up to ≈ 10 and ≈ 30 times larger respectively. If literature data are added to the GMASS sample, we find that only a few passive systems at $1.2 < z < 2.5$ lie within the $z \approx 0$ size-mass relation, whereas the majority has systematically much smaller sizes.
- The Kormendy relation at $z \approx 1.5$ shows a large offset (2–3 mag) in effective surface brightness with respect to the local relation. This is difficult to explain with simple luminosity evolution models and requires that these high- z compact and dense galaxies increase their size in order to reach the local Kormendy relation.
- Samples of ETGs at lower redshifts ($0.7 < z < 1.2$) show that a larger fraction of passive galaxies follow the $z \sim 0$ size-mass relation with respect to $z > 1.3$. The ETGs at $z \approx 1$ which have the largest offsets with respect to the $z \sim 0$ size-mass relation are the ones having the highest internal velocity dispersion, as expected from the ETG scaling relations. We find a hint that, for a fixed redshift $z \approx 1$, ETGs located within massive clusters are more preferentially located within the $z \sim 0$ size-mass relation than ETGs located in lower density environments.
- Superdense massive ETGs with $R_e \approx 1$ kpc are extremely rare at $z \approx 0$ with respect to $z > 1$, and absent if $R_e < 1$ kpc. However, it might be possible that compact and dense remnants are “hidden inside present-day ETGs if the size of ETGs grew through mechanisms such as the “smooth envelope accretion”.
- Submillimeter-selected galaxies are the only systems at $z \gtrsim 2$ with sizes and mass surface densities (in gas) similar to those of the passive galaxies at $z \approx 1$ –2. This suggests that a strong evolutionary link is present between these two galaxy populations.
- It is currently unclear how the possible link between SMGs and compact passive galaxies fits within a more general framework which takes into account also the other galaxy populations so far identified at $1 < z < 3$. A plausible scenario could be outlined as follows and summarized in Fig. 23. (1) Massive star-forming galaxies selected in the optical/near-IR are gas-rich disk systems with long-lived star formation (e.g. ≈ 0.5 –1 Gyr, Daddi et al. 2005b). (2) These systems can become unstable (e.g. Genzel et al. 2006) or participate in major merger events with other gas-rich systems. (3) In both cases a major starburst event is triggered, and this phase could correspond to the SMG stage characterized by short-lived (≈ 0.1 Gyr) vigorous starburst (Tacconi et al. 2006, 2007). (4) The concomitant AGN provides enough feedback to “quench” the star formation in massive systems (Daddi et al. 2007a), and (5) compact, superdense, passively evolving remnants are formed, (6) and evolve subsequently by increasing gradually their sizes with mechanisms like major dry merging and/or envelope accretion more or less rapidly depending on their mass and environment. (7) The majority of most massive ETGs reach the assembly completion around $z \approx 0.7$, while lower mass ETGs continue to assemble down to lower redshifts (downsizing).
- Larger samples in the range of $1 < z < 3$ are needed to place stringent constraints on the mechanism(s) with which the sizes of high- z passive galaxies grow as a function of cosmic time (e.g. dissipationless merging, envelope accretion, ...).

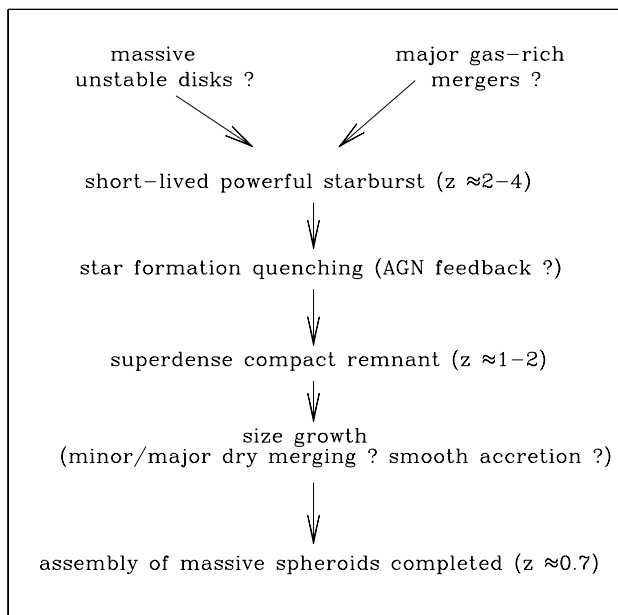


Fig. 23. A possible scenario for the formation and evolution of a massive spheroidal galaxy (see text).

High-resolution spectroscopy in the near-infrared with the next generation of telescopes (e.g. E-ELT, JWST) will also be crucial to study the internal dynamics of these systems. Further studies at $1 < z < 3$ will shed light on the global processes which lead to formation and evolution of massive galaxies.

Acknowledgements. We acknowledge the referee, Olivier Le Fevre, for the useful and constructive comments. We thank ESO for the generous allocation of observing time through the VLT Large Program 173.A-0687. We thank Mariangela Bernardi, Joel Brinchmann, Pat McCarthy, Georg Feulner, and Sadegh Khochfar for providing respectively unpublished information on SDSS galaxies with $\sigma_V > 350 \text{ km s}^{-1}$, the SDSS stellar masses, the GDDS composite spectra, the data on *SSFR*, and the model predictions. Sadegh Khochfar, Thorsten Naab, Luca Ciotti, Carlo Nipoti and Gabriella De Lucia are acknowledged for the helpful discussion. AC is particularly grateful to Reinhard Genzel, Linda Tacconi and Natascha Förster-Schreiber for the warm hospitality at Max-Planck-Institut für Extraterrestrische Physik and the stimulating discussions. AC acknowledges support through a *Bessel Prize* of the *Alexander von Humboldt Foundation*.

References

Abraham, R., Nair, P., McCarthy, P. J., et al. 2007, *ApJ*, in press
 Alexander, D. M., Bauer, F. E., Brandt, W. N., et al. 2003, *AJ*, 126, 539
 Arnouts, S., Walcher, C. J., Le Fevre, O., et al. 2007, *A&A*, 476, 137
 Beckwith, S. V. W., Stiavelli, M., Koekemoer, A. M., et al. 2006, *AJ*, 132, 1729
 Bell, E., Naab, T., McIntosh, D. H., et al. 2006, *ApJ*, 640, 241
 Bernardi, M., Sheth, R. K., Nichol, R. C., et al. 2006, *AJ*, 131, 2018
 Bernardi, M., Fritz, A., Hyde, J. B., et al. 2007, in preparation
 Berta, S., Lonsdale, C. J., Siana, B., et al. 2007, *ApJ*, submitted
 Bertin, E., & Arnouts, S. 1997, *A&AS*, 117, 393
 Blain, A. W., Smail, I., Ivison, R. J., Kneib, J.-P., & Frayer, D. T. 2002, *PhR*, 369, 111
 Blain, A. W., Chapman, S. C., Smail, I., & Ivison, R. 2004, *ApJ*, 611, 725
 Boylan-Kolchin, M., Ma, C.-P., & Quataert, E. 2006, *MNRAS*, 369, 1081
 Bournaud, F., Jog, C. J., & Combes, F. 2007, *A&A*, in press
 Borch, A., Meisenheimer, K., Bell, E., et al. 2005, *A&A*, 453, 869
 Borys, C., Chapman, S., Halpern, M., & Scott, D. 2003, *MNRAS*, 344, 385
 Bouché, N., Cresci, G., Davies, R., et al. 2007, *ApJ*, in press
 Brown, M. J. I., Dey, A., Jannuzi, B. T., et al. 2006, *ApJ*, 654, 858
 Brusa, M., Comastri, A., Daddi, E., et al. 2002, *ApJ*, 581, L89
 Bruzual, G. 2007, *Stellar populations as building blocks of galaxies*, ed. A. Vazdekis, & R. Peletier (Cambridge: Cambridge University Press), in press, *Proc. IAU Symp.*, 241 [arXiv:astro-ph/0703052]

Bruzual, G., & Charlot, S. 2003, *MNRAS*, 344, 1000
 Bundy, K., Ellis, R. S., Conselice, C. J., et al. 2006, *ApJ*, 651, 120
 Bundy, K., Treu, T., & Ellis, R. S. 2007, *ApJ*, 665, L5
 Cassata, P., Cimatti, A., Franceschini, A., et al. 2005, *MNRAS*, 357, 903
 Castellano, M., Salimbeni, S., Trevese, D., et al. 2007, *ApJ*, in press
 Chabrier, G. 2003, *PASP*, 115, 763
 Chapman, S., Blain, A. W., Smail, I., & Ivison, R. J. 2005, *ApJ*, 622, 772
 Charlot, S., & Bruzual, G. 2007, in preparation
 Chary, R., & Elbaz, D. 2001, 556, 562
 Cimatti, A., Mignoli, M., Daddi, E., et al. 2002, *A&A*, 392, 395
 Cimatti, A., Daddi, E., Renzini, A., et al. 2004, *Nature*, 430, 184
 Cimatti, A., Daddi, E., & Renzini, A. 2006, *A&A*, 453, L29
 Ciotti, L., Lanzoni, B., & Volonteri, M. 2007, *ApJ*, 658, 65
 Cotter, G., Simpson, C., & Bolton, R. C. 2005, *MNRAS*, 360, 685
 Cowie, L. L., Songaila, A., Hu, E. M., & Cohen, J. G. 1996, *AJ*, 112, 839
 Daddi, E., Cimatti, A., Pozzetti, L., et al. 2000, *A&A*, 361, 535
 Daddi, E., Cimatti, A., Renzini, A., et al. 2004b, *ApJ*, 617, 746
 Daddi, E., Renzini, A., Pirzkal, N., et al. 2005a, *ApJ*, 626, 680
 Daddi, E., Dickinson, M., Chary, R., et al. 2005b, *ApJ*, 631, L13
 Daddi, E., Dickinson, M., Morrison, G., et al. 2007a, *ApJ*, in press
 Daddi, E., Alexander, D. M., Dickinson, M., et al. 2007b, *ApJ*, in press
 De Lucia, G., Springel, V., White, S. D. M., et al. 2006, *MNRAS*, 366, 499
 di Serego Alighieri, S., Vernet, J., Cimatti, A., et al. 2005, *A&A*, 442, 125
 Dominguez-Tenreiro, R., Oñorbe, J., Sáiz, A., Artal, H., & Serna, A. 2006, *ApJ*, 636, L77
 Drory, N., Bender, R., & Hopp, U. 2004, *ApJ*, 616, L103
 Dunlop, J., Peacock, J., Spinrad, H., et al. 1996, *Nature*, 381, 581
 Faber, S. M., Willmer, C. N. A., Wolf, C., et al. 2007, *ApJ*, 665, 265
 Farrah, D., Lonsdale, C. J., Borys, C., et al. 2006, *ApJ*, 641, L17
 Feulner, G., Gabasch, A., Salvato, M., et al. 2005, *ApJ*, 633, L9
 Firth, A. E., Somerville, R. S., McMahon, R. G., et al. 2002, *MNRAS*, 332, 617
 Fontana, A., Pozzetti, L., Donnarumma, I., et al. 2004, *A&A*, 424, 23
 Förster Schreiber, N. M., Genzel, R., Lehnert, M. D., et al. 2006, *ApJ*, 645, 1062
 Franceschini, A., Rodighiero, G., Cassata, P., et al. 2006, *A&A*, 453, 397
 Franx, M., Labbé, I., Rudnick, G., et al. 2003, *ApJ*, 587, L79
 Gavazzi, G., & Scoddeggio, M. 1996, *A&A*, 312, L29
 Genzel, R., Tacconi, L. J., Eisenhauer, F., et al. 2006, *Nature*, 442, 786
 Giacconi, R., Zirm, A., Wang, J., et al. 2002, *ApJS*, 139, 369
 Giallisco, M., Ferguson, H. C., Koekemoer, A. M., et al. 2004, *ApJ*, 600, L93
 Glazebrook, K., Abraham, R. G., McCarthy, P. J., et al. 2004, *Nature*, 430, 181
 Granato, G., De Zotti, G., Silva, L., et al. 2004, *ApJ*, 600, 580
 Jorgensen, I., Franx, M., & Kjaergaard, P. 1995, *MNRAS*, 273, 1097
 Juneau, S., Glazebrook, K., Crampton, D., et al. 2005, *ApJ*, 619, L135
 Kauffmann, G., Heckman, T. M., White, S. D. M., et al. 2003, *MNRAS*, 341, 33
 Kennicutt, R. 1998, *ARA&A*, 36, 189
 Khochfar, S., & Silk, J. 2006a, *MNRAS*, 370, 902
 Khochfar, S., & Silk, J. 2006b, *ApJ*, 648, L21
 Kong, X., Daddi, E., Arimoto, N., et al. 2006, *ApJ*, 638, 72
 Kriek, M., van Dokkum, P. G., Franx, M., et al. 2006, *ApJ*, 649, L71
 Kroupa, P. 2001, *MNRAS*, 322, 231
 Kurk, J., et al. 2007a, in preparation
 Kurk, J., et al. 2007b, in preparation
 Law, D. R., Steidel, C. C., Erb, D. K., et al. 2007, *ApJ*, in press
 Longhetti, M., Saracco, P., Severgnini, P., et al. 2005, *MNRAS*, 361, 897
 Longhetti, M., Saracco, P., Severgnini, P., et al. 2007, *MNRAS*, 374, 614
 Maraston, C. 1998, *MNRAS*, 300, 872
 Maraston, C. 2005, *MNRAS*, 362, 799
 Maraston, C., Daddi, E., Renzini, A., et al. 2006, *ApJ*, 652, 85
 Masjedi, M., Hogg, D., Cool, R. J., et al. 2006, *ApJ*, 644, 54
 Masjedi, M., Hogg, D., & Blanton, M. R. 2007, *ApJ*, submitted
 McCarthy, P. J., Le Borgne, D., Crampton, D., et al. 2004, *ApJ*, 614, L9
 McCarthy, P. J., Yan, H., Abraham, R. G., et al. 2007, *ApJ*, 664, L17
 McGrath, E. J., Stockton, A., & Canalizo, G. 2007, *ApJ*, in press
 McGrath, E., Stockton, A., Canalizo, G., Iye, M., & Maihara, T. 2007, *ApJ*, submitted
 McIntosh, D. H., Bell, E. F., Rix, H.-W., et al. 2005, *ApJ*, 632, 191
 Menci, N., Fontana, A., Giallongo, E., Grazian, A., & Salimbeni, S. 2006, *ApJ*, 647, 753
 Mignoli, M., Cimatti, A., Zamorani, G., et al. 2005, *A&A*, 437, 883
 Naab, T., Johansson, P. H., Ostriker, J. P., & Efstathiou, G. 2007, *ApJ*, 658, 710
 Narayanan, D., Cox, T. J., Robertson, B., et al. 2006, *ApJ*, 642, L107
 Nipoti, C., Londrillo, P., & Ciotti, L. 2003a, *MNRAS*, 342, 501
 Nipoti, C., Stiavelli, M., Ciotti, L., Treu, T., & Rosati, P. 2003b, *MNRAS*, 344, 748
 Peletier, R. F., Davies, R. L., Illingworth, G. D., Davis, L. E., & Cawson, M. 1990, *AJ*, 100, 1091
 Peng, C. Y., Ho, L. C., Impey, C. D., & Rix, H.-W. 2002, *AJ*, 124, 266

- Perez-Gonzalez, G., Rieke, G. H., Villar, V., et al. 2007, *ApJ*, in press [arXiv:0709.1354]
- Pirzkal, N., Xu, C., Malhotra, S., et al. 2004, *ApJS*, 154, 501
- Ponder, J. M., Burstein, D., O'Connell, R. W., et al. 1998, *AJ*, 116, 2297
- Pozzetti, L., Cimatti, A., Zamorani, G., et al. 2003, *A&A*, 402, 837
- Pozzetti, L., Bolzonella, M., Lamareille, F., et al. 2007, *A&A*, 474, 443
- Renzini, A. 1981, *Ann. Phys. Fr.* 6, 87
- Renzini, A. 2006, *ARA&A*, 44, 141
- Rettura, A., Rosati, P., Strazzullo, V., et al. 2006, *A&A*, 458, 717
- Rodighiero, G., Gruppioni, C., Civano, F., et al. 2007, *MNRAS*, 376, 416
- Salpeter, E. E. 1955, *ApJ*, 121, 161
- Saracco, P., Longhetti, M., Severgnini, P., et al. 2005, *MNRAS*, 372, L40
- Scarlata, C., Carollo, C. M., Lilly, S. J., et al. 2007, *ApJS*, 172, 494
- Scott, S. E., Fox, M. J., Dunlop, J. S., et al. 2002, 331, 817
- Shapley, A., Erb, D. K., Pettini, M., Steidel, C. C., & Adelberger, K. L. 2004, *ApJ*, 612, 108
- Shen, S., Mo, H. J., White Simon, D. M., et al. 2003, *MNRAS*, 343, 978
- Spinrad, H., Dey, A., Stern, D., et al. 1997, *ApJ*, 484, 581
- Swinbank, A. M., Chapman, S. C., Smail, I., et al. 2006, *MNRAS*, 465
- Tacconi, L., Neri, R., Chapman, S. C., et al. 2006, *ApJ*, 640, 228
- Tacconi, L., Genzel, R., Smail, I., et al. 2007, *ApJ*, submitted
- Thompson, R. I., Illingworth, G., Bouwens, R., et al. 2005, *AJ*, 130, 1
- Toft, S., van Dokkum, P., Franx, M., et al. 2007, *ApJ*, in press
- Totani, T. I., Yoshii, Y., Iwamuro, F., et al. 2001, *ApJ*, 558, L87
- Trujillo, I., Feulner, G., Goranova, Y., et al. 2006, *MNRAS*, 373, L36
- Trujillo, I., Conselice, C., Bundy, K., et al. 2007, *MNRAS*, in press
- van Dokkum, P. 2005, *AJ*, 130, 2647
- van Dokkum, P., & Stanford, S. A. 2003, *ApJ*, 585, 78
- Vanzella, E., Cristiani, S., Dickinson, M., et al. 2006, *A&A*, 454, 423
- Yamada, T., Kodama, T., Kobayashi, Y., et al. 2005, *ApJ*, 634, 861
- Yan, H., Dickinson, M., Eisenhardt, P., et al. 2004, *ApJ*, 616, 63
- Yan, R., Newman, J. A., Faber, S. M., et al. 2006, *ApJ*, 648, 281
- Wright, S. A., Larkin, J. E., Barczys, M., et al. 2007, *ApJ*, 655, 51
- Wuyts, S., Labbé, I., Franx, M., et al. 2007, *ApJ*, 655, 51
- Zirm, A. W., van der Wel, A., Franx, M., et al. 2007, *ApJ*, 656, 66